



# Kinematics of the lever arm swing in myosin VI

Mauro L. Mugnai<sup>a,b,1,2</sup> and D. Thirumalai<sup>a,b,1,2</sup>

<sup>a</sup>Biophysics Program, Institute for Physical Science and Technology, University of Maryland, College Park, MD 20742; and <sup>b</sup>Department of Chemistry and Biochemistry, University of Maryland, College Park, MD 20742

Edited by Michael L. Klein, Temple University, Philadelphia, PA, and approved April 5, 2017 (received for review September 20, 2016)

**Myosin VI (MVI) is the only known member of the myosin superfamily that, upon dimerization, walks processively toward the pointed end of the actin filament. The leading head of the dimer directs the trailing head forward with a power stroke, a conformational change of the motor domain exaggerated by the lever arm. Using a unique coarse-grained model for the power stroke of a single MVI, we provide the molecular basis for its motility. We show that the power stroke occurs in two major steps. First, the motor domain attains the poststroke conformation without directing the lever arm forward; and second, the lever arm reaches the poststroke orientation by undergoing a rotational diffusion. From the analysis of the trajectories, we discover that the potential that directs the rotating lever arm toward the poststroke conformation is almost flat, implying that the lever arm rotation is mostly uncoupled from the motor domain. Because a backward load comparable to the largest interhead tension in a MVI dimer prevents the rotation of the lever arm, our model suggests that the leading-head lever arm of a MVI dimer is uncoupled, in accord with the inference drawn from polarized total internal reflection fluorescence (polTIRF) experiments. Without any adjustable parameter, our simulations lead to quantitative agreement with polTIRF experiments, which validates the structural insights. Finally, in addition to making testable predictions, we also discuss the implications of our model in explaining the broad step-size distribution of the MVI stepping pattern.**

myosin VI | power stroke | coarse-grained simulations | uncoupled lever arm swing | quantitative experimental predictions

Like their counterparts dyneins and kinesins, myosins are molecular motors that transform chemical energy harvested in the hydrolysis of ATP into mechanical work. They do so by undergoing a reaction cycle (Fig. 1) involving ATP hydrolysis coupled with binding to and unbinding from the filamentous actin (F-actin) (1, 2). Myosins loaded with a hydrolyzed ATP bind to F-actin, release the products of ATP hydrolysis, and undergo a structural change known as a power stroke. The structural change of the N-terminal part of the motor domain, where the actin and nucleotide binding sites reside, is communicated to the converter domain that moves from the prepower stroke (PrePS) state to the postpower stroke (or rigor, R) state conformation. The movement of the converter is exaggerated by the large swing of the lever arm, an oblong domain bound to light chains or calmodulins (CaMs). When a new ATP molecule binds the nucleotide-free myosin (in the R state), the motor detaches from actin and it is ready to begin a new cycle.

Much of the work on nonmuscle myosins has focused on myosin V (MV). However, since the discovery that myosin VI (MVI) has an unusual structure, there has been an increasing interest in the motility of MVI. In addition to its biophysical importance, MVI has been implicated in a wide variety of cellular functions in different organisms (3, 4). For instance, MVI is involved in endocytosis, spermatogenesis, cell migration, the organization of the cytoskeleton and the Golgi apparatus, and protein localization. It also plays a role in the maintenance of stereocilia of the inner ear cell. Mutations of the *myo6* gene induce deafness in mice and in humans (3). The effect of a deafness-inducing mutation on the MVI cycle has been elucidated recently, thus suggesting a mech-

anism by which the functioning of the mutant is hampered (5). MVI is overexpressed in cancerous ovarian cells, and the inhibition of its expression reduces the tumor propensity to disseminate (6). MVI is also overexpressed in cancerous prostate cells (7).

Some myosins perform their physiological function as monomers, and others form dimers that walk processively, i.e., they take multiple consecutive steps on the polar track F-actin, without detaching. MVI, monomeric in solution (8), can form dimers (9–13) capable of processive movement (9, 10).

Processive motors display high duty ratio (the motor spends most of its cycle tightly bound to F-actin), gating (communication between two heads), and a power stroke (2). Although gating in a high duty ratio motor might not be necessary, it is likely to increase motor efficiency and run length (14). A recent coarse-grained model of MVI provided structural evidence that ADP release is gated (15), in agreement with experiments (16) and kinetic models (14), although it was also proposed that blocking ATP binding constitutes the gating mechanism in MVI (17).

In addition to displaying gating and a high duty ratio (17, 18), MVI shows a number of striking features that distinguish it from other processive myosins, such as the well-studied MV: (i) For starters, whereas MV and all other members of the myosin superfamily move toward the barbed end (or plus end) of F-actin, MVI steps toward the pointed end (or minus end) (2, 19). (ii) The lever arm architecture differs significantly between MV and MVI (20). In MV there are six CaMs or light-chain-bound IQ domains that constitute the lever arm, with length that is commensurate with the 36-nm spacing in the F-actin repeat. MVI has only one IQ domain, but in a step covers the same distance as MV, suggesting that other elements contribute to the lever arm. Although their origin remains unclear (20–26), recent studies investigating MVI function suggest the importance of the proximal tail as a lever arm extension in vivo (27). (iii) Furthermore, the step-size

## Significance

**Myosin VI (MVI), a molecular motor whose malfunction is linked to deafness, moves on the actin filament fueled by ATP. The chemomechanical transduction culminates in a power stroke, in which the motor domain undergoes a conformational transition exaggerated by the lever arm. We performed simulations of the MVI power stroke, showing that the lever arm undergoes a nearly free rotational diffusion that is only weakly biased by the rest of the motor. Our model yields a molecular picture of the MVI power stroke that is in quantitative agreement with experiments showing evidence for the pliancy of the lever arm. Our findings provide insights into the broad step-size distribution of MVI.**

Author contributions: M.L.M. and D.T. designed research; M.L.M. performed research; M.L.M. and D.T. analyzed data; and M.L.M. and D.T. wrote the paper.

The authors declare no conflict of interest.

This article is a PNAS Direct Submission.

<sup>1</sup>Present address: Department of Chemistry, The University of Texas at Austin, Austin, TX 78712.

<sup>2</sup>To whom correspondence may be addressed. Email: dave.thirumalai@gmail.com or mauro1m83@gmail.com.

This article contains supporting information online at [www.pnas.org/lookup/suppl/doi:10.1073/pnas.1615708114/-DCSupplemental](http://www.pnas.org/lookup/suppl/doi:10.1073/pnas.1615708114/-DCSupplemental).

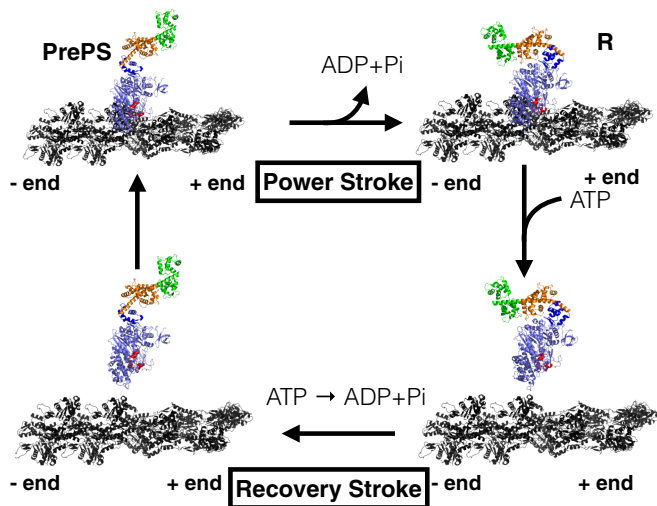


**Fig. 1.** The reaction cycle of MVI. Color code: slate blue, motor domain; red, ins1; dark blue, converter; orange, ins2 and ins2-bound CaM; green, IQ domain and IQ-bound CaM; black, actin. The Protein Data Bank (PDB) structures used to make this figure are 4ANJ (41) and 2BK1 (33) for the motor domain, the MVI lever arm was extracted from 3GN4 (23), and the F-actin was adopted from 1MVW (48). Both PrePS and R models were aligned against a myosin bound to actin in 1MVW.

distribution of the wild-type MV is much narrower than in MVI (9, 10, 20). (iv) And finally, both MV and MVI move processively by a hand-over-hand mechanism (28–30), but in MVI there is also evidence of inchworm-like steps (31).

Most of the unconventional mechanical properties of MVI are attributed to insert 1 and insert 2 (ins1 and ins2) (Fig. 2), two unique fragments within the myosin superfamily (19). Single-molecule experiments (32) and crystal structures of the R (33) and PrePS (34) states indicated ins2 as the key structural element responsible for the reversal of MVI directionality during stepping. Indeed, ins2 wraps around the converter domain, effectively turning the direction of the swing backward, and its removal changes the directionality of MVI motion. Kinetics experiments suggest that ins1 plays a key role in determining MVI high duty ratio and gating (17, 35).

Some of the essential features of the MVI stepping mechanism are not fully understood, including the unusually large step-size distribution and the alternation between hand-over-hand and inchworm steps. Although models of the dimer incorporating the flexibility of the MVI lever arm are capable of reproducing known features of MVI motility (36), experiments using a chimeric MVI with the MV lever arm showed that the step-size distribution was similar to the wild type (32, 37), suggesting that the elusive structure of the MVI lever arm might not be the key ingredient needed to explain the peculiar stepping mechanism of MVI. Following experimental studies, structural modeling, and simulations, it is tempting to conclude that the uncoupling of the MVI leading-head lever arm from the movement of the converter, or the pliancy of the lever arm, and the conformational transition in the converter may contribute to the large step-size distribution (30, 38–41). Furthermore, according to a recently proposed model (31, 37), short steps occur if the free, trailing head of a myosin dimer binds F-actin while the lever arm of the actin-bound, leading head remains in the prestroke orientation. Conversely, a rotation of the bound-head lever arm to the R-state orientation results in large steps.

Although experimental evidence supports the model of the uncoupling or pliancy of the lever arm (30, 38–41), direct evidence requires a structural model capable of describing the dynamics of the lever arm swing. We use a combination of

coarse-grained (CG) simulations and theory to probe the dynamics of the swing of the lever arm in MVI. In recent years, numerous simulations on a variety of systems have shown the reliability of CG models in extracting the salient features of the dynamics of macromolecules (42–47). We prepared a model for the PrePS and R conformation that includes the lever arm up to ins2 and the IQ domain (Fig. 2*B* and *C*). We modeled the power stroke by inducing the transition from the PrePS to the R conformation, ignoring any intermediate configuration and F-actin (see *Materials and Methods* for a fuller discussion). We generated 96 trajectories of the PrePS→R transition to study the power stroke—for a discussion about the convergence of the results see *SI Appendix, section 4* and *SI Appendix, Fig. S14*. To understand the effect of backward load on the rotation of the lever arm, we generated 96 trajectories of the PrePS→R transition with the lever arm subject to a resistive force of 6 pN. Our results suggest that the PrePS→R transition occurs in two major steps: In the first step, the motor domain reaches the R state, while the lever arm is uncoupled. In the second step, the lever arm diffuses toward the R-state configuration with a small guidance from the motor domain. Our model leads us to propose that the inchworm-like steps might occur when the free head binds F-actin before the uncoupled lever arm rotates to the R-state conformation, which identifies a direct connection between short (or inchworm-like) steps and the uncoupling of the lever arm. The results of our simulations not only compare favorably with experiments, but also yield precise, testable predictions.

## Results

**The Lever Arm Rotation Occurs in Two Major Steps.** We monitor the dynamics of the PrePS→R transition using the structural overlap function ( $\chi$ ) with respect to the R state given by (49)

$$\chi(t) = \frac{2}{N_B^2 - 5N_B + 6} \sum_{i=1}^{N_B-3} \sum_{j=i+3}^{N_B} \Theta(|r_{ij}(t) - r_{ij}(R)| - a), \quad [1]$$

where  $N_B$  is the number of beads in the CG model (excluding those that were not resolved in the crystal structure, see *SI Appendix, section 1*),  $r_{ij}(t)$  is the distance between the beads  $i$  and  $j$  at time  $t$ ,  $r_{ij}(R)$  is the distance in the R state,  $\Theta$  is the Heaviside function, and  $a = 2 \text{ \AA}$  is the tolerance. The summation in Eq. 1 is over pairs of beads that are at least three residues apart in the sequence (the total number of such pairs is the inverse of the prefactor in Eq. 1). In the PrePS state,  $\chi \approx 0.62$ , and in the R state,  $\chi \approx 0.34$ . The time trace of  $\chi$  shows that the PrePS→R transition occurs in two steps (black line in Fig. 3*A*). Within a few microseconds,  $\chi$  decreases to  $\approx 0.55$  (Fig. 3*A, Inset*) and it fluctuates around this value for a long time until it undergoes another rapid transition leading to the R state. The structural overlap function fluctuates around 0.34 until the end of the simulation. Similar patterns are found in all of the trajectories.

Let us refer to the time of the completion of the first step as  $\tau_{\chi 1}$ , the time to the beginning of the second step as  $\tau_{\chi 2}$ , and the time to complete the second step as  $\tau_{\chi 3}$ . In practice,  $\tau_{\chi 1}$  ( $\tau_{\chi 3}$ ) is measured as the first time  $\chi$  reached 0.55 (0.34) (red and blue arrows in Fig. 3*A*). The time at which the second step begins,  $\tau_{\chi 2}$ , is measured as the last time the trajectory crosses 0.55 before reaching 0.34 (green arrow in Fig. 3*A*). The histograms of  $\tau_{\chi 1}$ ,  $\tau_{\chi 2} - \tau_{\chi 1}$ , and  $\tau_{\chi 3} - \tau_{\chi 2}$  are shown in Fig. 3*B*. Note the difference in the scale of the abscissa. Clearly, the first transition occurs rapidly ( $\tau_{\chi 1}$  average is  $\langle \tau_{\chi 1} \rangle = 2.6 \mu\text{s}$ , with SD  $\sigma_{\tau_{\chi 1}} = 1.2 \mu\text{s}$ ), followed by a long waiting time ( $\langle \tau_{\chi 2} - \tau_{\chi 1} \rangle = 178 \mu\text{s}$ ,  $\sigma_{\tau_{\chi 2} - \tau_{\chi 1}} = 122 \mu\text{s}$ ) before another rapid transition ( $\langle \tau_{\chi 3} - \tau_{\chi 2} \rangle = 4.9 \mu\text{s}$ ,  $\sigma_{\tau_{\chi 3} - \tau_{\chi 2}} = 2.4 \mu\text{s}$ ). The origin of the large distribution of  $\tau_{\chi 2} - \tau_{\chi 1}$  is discussed in the next section.

**Structural Transitions During the Two Steps.** To characterize the structural origin of the two steps observed in the time trace of

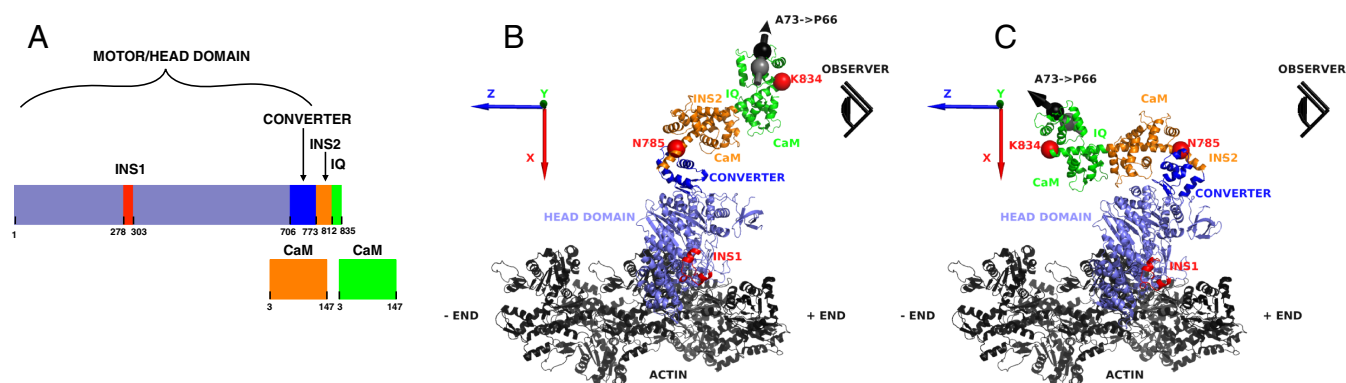


**Fig. 2.** Sequence and structural models of MVI. (A) Sequence of the modeled MVI with bound CaMs. (B and C) PrePS (B) and R (C) models used in the simulations. The color code is the same as in Fig. 1. The total number of residues in the protein is 834. Each CaM has 145 residues. The total number of residues for our PrePS and R models is 1,124. F-actin was not part of the model, but it is shown here for reference. The red spheres show the residues N785 and K834, the beginning and the end of the lever arm in our model. The gray and black spheres show P66 and A73 of the IQ-bound CaM. The size of the four spheres is exaggerated to enhance visibility. In ref. 38 a bifunctional rhodamine used to reveal the orientation of the lever arm is attached to these two residues. The three axes,  $\hat{x}$ ,  $\hat{y}$ , and  $\hat{z}$  are shown as a red, a green, and a blue arrow, respectively. The position of the observer is shown pictorially as an eye. The observer stands on F-actin behind MVI, parallel to the  $\hat{x}$  axis and oriented in the negative direction, looking toward the pointed end of the filament.

$\chi(t)$  during the PrePS $\rightarrow$ R transition, we monitor the following three distances between beads that form contacts in the R state, but not in the PrePS state: (i) dRED is the distance between C63 and R708 (red spheres in Fig. 4), (ii) dGREEN is the distance between T754 and D24 of the ins2-bound CaM (green spheres in Fig. 4), and (iii) dBLUE is the distance between V140 and D58 of the ins2-bound CaM (blue spheres in Fig. 4). When the converter moves from the PrePS to the R-state conformation, the dRED contact is formed. The formation of the dGREEN contact indicates the initial closure of the lever arm onto the motor domain, which is completed when the dBLUE contact is formed. The time traces of these three distances for a particular trajectory are shown in Fig. 3A, from which it appears that the formation of the dRED contact coincides with the first step in the decrease of  $\chi(t)$  and the second step of  $\chi(t)$  occurs around the same time when dGREEN and dBLUE are formed. To determine whether this observation holds for all trajectories, we extract from each trajectory the time for stable formation of the three contacts. By stable we mean that once the contact is formed, it remains

intact with small fluctuations (in practice, we monitor stable contacts by checking the first time at which the contact is formed such that for the rest of the simulation the contact stays closer to the R-state ideal distance than to the largest distance explored during the PrePS $\rightarrow$ R transition). We refer to the time for stable formation of dRED, dGREEN, and dBLUE as  $t_1$ ,  $t_2$ , and  $t_3$ , respectively, and we investigate the correlations between  $t_1$  and  $\tau_{\chi_1}$ ,  $t_2$  and  $\tau_{\chi_2}$ , and  $t_3$  and  $\tau_{\chi_3}$ . Fig. 5A shows that there is good correlation between  $t_1$  and  $\tau_{\chi_1}$ , with the exception of a few solid circles, which represent all those trajectories in which the lever arm begins to close onto the motor domain before the rotation of the converter domain occurs, that is, before dRED is formed. In these cases, the initial drop in  $\chi(t)$  reflects the formation of the dGREEN contact. In three of five cases (blue solid circles in Fig. 5A), the initial dGREEN contact is transitory, which means that it rapidly breaks, the converter rotates, and it finally reforms; thus ultimately the stable formation of the dRED contact precedes the dGREEN contact. In the two cases shown as black solid circles in Fig. 5A the dGREEN contact is stably

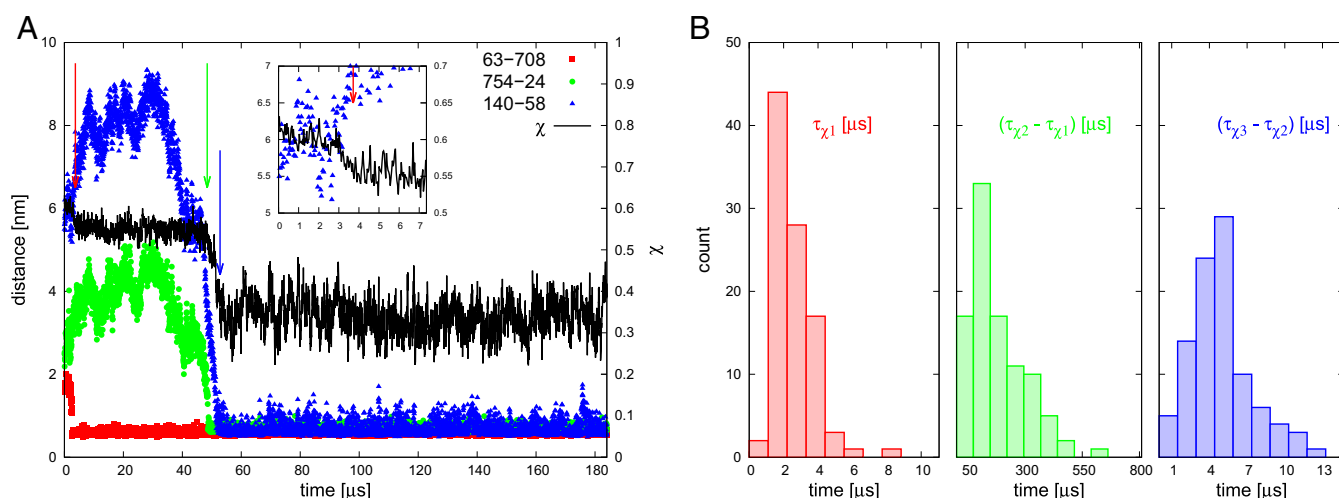


**Fig. 3.** Dynamics of the PrePS $\rightarrow$ R transition. (A) The dependence of  $\chi$  on time is in black. The red arrow indicates the end of the first transition, and the green and blue arrows correspond to the start and end of the second transition, respectively. A also shows the time traces of the distance between C63 and R708 (red squares), T754 and D24 of the ins2-bound CaM (green circles), and V140 and D58 of the ins2-bound CaM (blue triangles). A, Inset shows the initial transition in  $\chi$ . (B, Left) Histogram of  $\tau_{\chi_1}$ . (B, Center) Histogram of  $\tau_{\chi_2} - \tau_{\chi_1}$ . (B, Right) Histogram of  $\tau_{\chi_3} - \tau_{\chi_2}$ . Here,  $\tau_{\chi_1}$  is the end of the first transition, and  $\tau_{\chi_2}$  and  $\tau_{\chi_3}$  are, respectively, the start and the end of the second transition monitored by  $\chi$ .

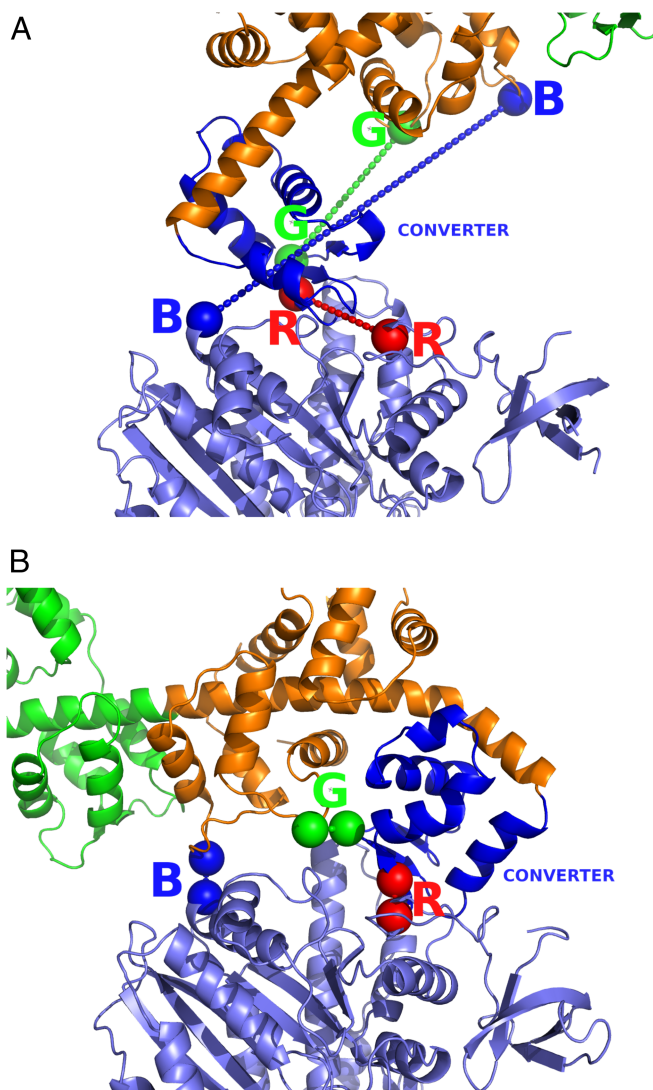


**Fig. 4.** Monitoring the key structural changes in the PrePS→R transition. The locations of the  $C_{\alpha}$  atoms of C63 and R708 are shown as red spheres, and those of T754 and D24 of the ins2-bound CaM are shown as green spheres. The blue spheres show the  $C_{\alpha}$  positions of V140 and D58 of the ins2-bound CaM, respectively. The dashed lines connect the beads involved in the dRED, dGREEN, and dBLUE contacts. To enhance visibility, the location of the spheres is also highlighted by a label R, G, or B. A shows the PrePS state, and B shows the R state.

formed before dRED, and it does not break. The Pearson correlation coefficient and the linear fit, performed in the absence of the solid circles, illustrates that in most cases (91/96 trajectories) dRED forms around  $\tau_{\chi 1}$ . This suggests that at  $t \approx \tau_{\chi 1}$  the converter is on the plus-end side of the MVI motor domain (Fig. 2 B and C). A close examination of the crystal structures before and after the PrePS→R transition (33, 34) reveals that the converter undergoes a rotation and also is subject to a conformational change from the so-called P-fold to the R-fold. The distance dRED can monitor only the translation of the converter, but we show in *SI Appendix*, sections 2 and 3 and *SI Appendix*, Figs. S6–S8 that around  $\tau_{\chi 1}$  the converter and the motor domain undergo the needed rotation and the structural transition to reach the R-state conformation. We deduce that, in most of the cases, the first step in the lever arm swing corresponds to the movement of the converter from the PrePS to the R configuration.

The Pearson correlations of  $t_2$  with  $\tau_{\chi 2}$  and of  $t_3$  with  $\tau_{\chi 3}$  are shown in Fig. 5 B and C. The two correlation coefficients are very close to unity, and the linear fit yields small intercepts (Fig. 5 legend). Hence, the dGREEN contact forms around  $\tau_{\chi 2}$ , followed by the formation of the dBLUE contact at  $t \approx \tau_{\chi 3}$ .

The analysis conducted so far monitoring  $\chi$  and the formation of the dRED, dGREEN, and dBLUE contacts suggests that we can divide our trajectories into two classes: (i) In most cases (91/96), the first step of  $\chi$  corresponds to a movement of the converter domain from the PrePS to the R position (formation of the dRED contact). Rarely (3/96), we observed that the movement of the converter is preceded by the transitory formation of a R-state contact between the lever arm and the motor domain (dGREEN contact). Once the converter has moved, after a long waiting time, ins2 closes onto the motor domain to form the R state (stable formation of dGREEN and dBLUE contacts). Hence, the first step is a power-stroke transition of the motor domain (including the converter), and during the second step the lever arm attains the R-state conformation. This suggests that, in all these trajectories (94/96), the movement of the lever arm is “uncoupled” from the PrePS→R transition of the converter. We refer to these trajectories as uncoupled. Examples of uncoupled trajectories are shown in *Movies S1 and S2* and *SI Appendix*, Figs. S11 and S18. (ii) In a minority of trajectories (2/96) an R-state-like stable contact between ins2 and the motor domain is formed before the switch of the position of the converter. These trajectories are classified as “coupled,” because in this mechanism the interaction between the lever arm and the motor domain leads to a rapid swing of the lever arm directed by the movement of the converter. *Movies S3 and S4* and *SI Appendix*, Figs. S12 and S19 show examples of coupled trajectories.

The number of coupled trajectories can be artificially increased by modifying the potential that induces the PrePS→R transition (*SI Appendix*, section 1 and *SI Appendix*, Figs. S2–S4). However, the conformation of the lever arm generated in the coupled trajectories did not reproduce the experimental data in ref. 38 (*SI Appendix*, section 1 and *SI Appendix*, Fig. S5). Hence, in the next two sections we focus our analysis exclusively on the uncoupled trajectories.

#### The Rotation of the Ins2-IQ Domain in the Uncoupled Trajectories.

The reference system is shown in Fig. 2 B and C. The  $\hat{z}$  axis is nearly parallel to the actin filament, with the minus end of F-actin directed toward the positive side of the axis. MVI is approximately parallel to the  $\hat{x}$  axis and oriented toward the negative direction. The view of the observer used as reference is described in Fig. 2 B and C. To follow the movement of the lever arm, we monitor the position of N785 (in ins2, shown as a red bead in Fig. 2 B and C) and K834 (last residues of the IQ domain, shown as a red bead in Fig. 2 B and C). Sample trajectories (*SI Appendix*, Figs. S9, S11, and S18 and *Movies S1 and S2*) show that N785 moves during  $t < \tau_{\chi 1}$  from the PrePS state nearly to the R-state configuration. When  $t$  exceeds  $\tau_{\chi 1}$ , it rapidly finds the R-state equilibrium position, fluctuating around this value for the rest of the simulation. On the other hand, K834 undergoes a large rotary movement around the converter from the value in the PrePS state to the one in the R state (*SI Appendix*, Figs. S9, S11, and S18 and *Movies S1 and S2*). We conclude that, after the initial step in the PrePS→R transition, N785 serves as the hinge around which the distal part of ins2 and the IQ domain rotate until they reach the R state. To monitor the rotation of the lever arm in the most intuitive way, we describe the vector connecting N785 to K834 in spherical coordinates. Because the distance between N785 and K834 is roughly constant during the PrePS→R transition (*SI Appendix*, Fig. S10, *Top*), we describe the movement to the R state of the uncoupled lever arm as a rigid rod rotation with changes in the altitudinal angle,  $\theta$ , and the azimuthal angle,  $\phi$  (Fig. 6A). Because the relevant motion of

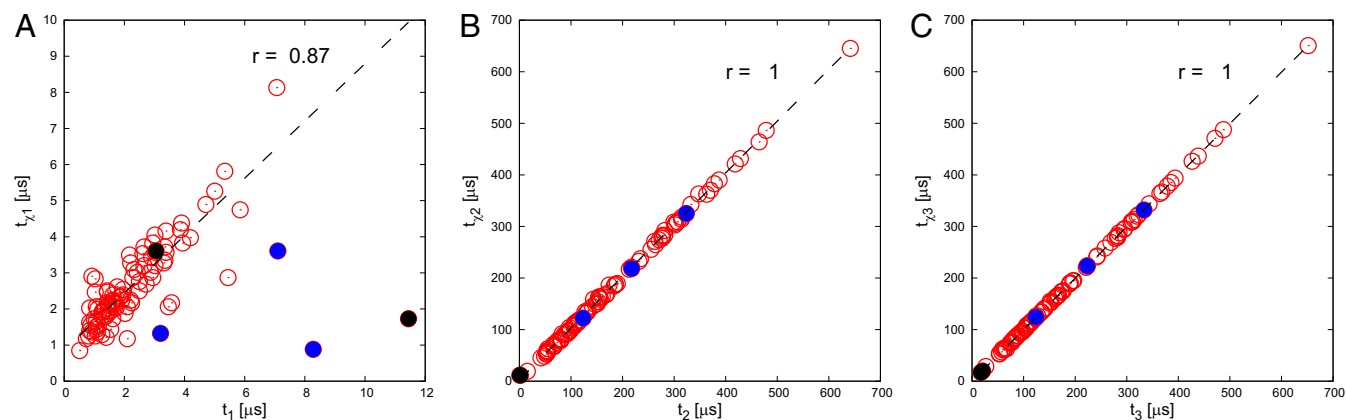


**Fig. 5.** Correlation between transition in  $\chi$  and the structural changes in MVI. (A) Plot of  $\tau_{\chi 1}$  against  $t_1$ . Blue (black) solid circles indicate results from simulations in which temporarily (permanently) the dGREEN contact forms before the dRED contact. The slope of the linear fit is  $\approx 0.78$ , whereas the intercept is  $\approx 0.86 \mu\text{s}$ . (B) Plot of  $\tau_{\chi 2}$  vs.  $t_2$ . The slope of the linear fit is  $\approx 1.00$ , and the intercept is  $\approx 2.6 \mu\text{s}$ . (C)  $\tau_{\chi 3}$  plotted against  $t_3$ . The slope of the linear fit is  $\approx 1.00$ , and the intercept is  $\approx 0 \mu\text{s}$ . The linear fits and the correlation coefficients are computed without the blue solid circles in A and with all of the circles in B and C.

the lever arm is in the direction of F-actin, we choose  $\theta$  as the order parameter and describe the dynamics of the lever arm on a unit circle.

**Energetics of the Lever Arm Swing.** The rotating lever arm is subject to a free energy  $F(\theta)$  that governs its motion. We extract this free energy from the trajectories to decipher the extent of the coupling between the lever arm and the motor domain. Assuming that at the start of the rotation the lever arm is at an angle  $\theta = \theta_i$  and at the end the altitudinal angle is  $\theta = \theta_f$ , and ignoring the role of the azimuthal angle, a large  $(F(\theta_i) - F(\theta_f)) \gg k_B T$ , downhill free energy suggests that the swing is guided. In contrast, if the free energy is flat  $(F(\theta_i) - F(\theta_f)) \approx k_B T$ , then the lever arm is uncoupled in the  $\theta$  direction. To extract the free energy  $F(\theta)$  we cannot simply compute the logarithm of the equilibrium probability distribution  $\rho(\theta)$ , because once the lever arm reaches the R state we do not observe transitions to the PrePS state. Hence, the system is out of equilibrium, and we need to adopt a different strategy to extract  $F(\theta)$ . We adopt a procedure put forward in ref. 50 (details in *SI Appendix, section 4*). We generate a stationary probability distribution on a unit circle  $\rho_r(\theta)$  from the simulated PrePS $\rightarrow$ R transitions. The trajectories

are injected at an angle  $\theta_i = 2.25$  rad (close to the PrePS state,  $\theta_{\text{PrePS}} \approx 2.55$  rad) and are removed when they cross  $\theta_f = 0.25$  rad (close to the R state,  $\theta_{\text{R}} \approx 0.04$  rad). We assume that the stationary probability  $\rho_r(\theta)$  is the solution of a Fokker-Planck (FP) equation subject to appropriate boundary conditions to account for the injection and removal of the trajectories (50). Because we know  $\rho_r(\theta)$  from simulations, we obtain the free energy  $F(\theta)$  by solving the FP equation. To solve the FP equation we assume that the diffusion coefficient  $D$  is a constant. In Fig. 6B we show the probability distribution  $\rho_r^{\text{CG}}(\theta)$  obtained from the analysis of the CG simulations (blue solid circles). As described in detail in *SI Appendix, section 4*, we fit the free energy  $F(\theta)$  to obtain a probability distribution  $\rho_r(\theta)$  (Fig. 6B, red line) that closely recovers the results from simulations.

The profile of  $F(\theta)$  shows that from  $\theta = 2.25$  rad ( $\approx 129^\circ$ ) to  $\theta \approx \pi/4$  ( $\approx 45^\circ$ ) a large part of the swing occurs on an almost flat free-energy profile (Fig. 6C). For  $\theta < \pi/4$  there is a shallow minimum of  $\approx 1$  kcal/mol, that drives the last part of the swing. We conclude that the swing occurs without a strong interaction with the motor domain, implying that the lever arm movement is mostly uncoupled, which is qualitatively revealed in the trajectories (*SI Appendix, Figs. S11 and S18 and Movies S1 and S2*).

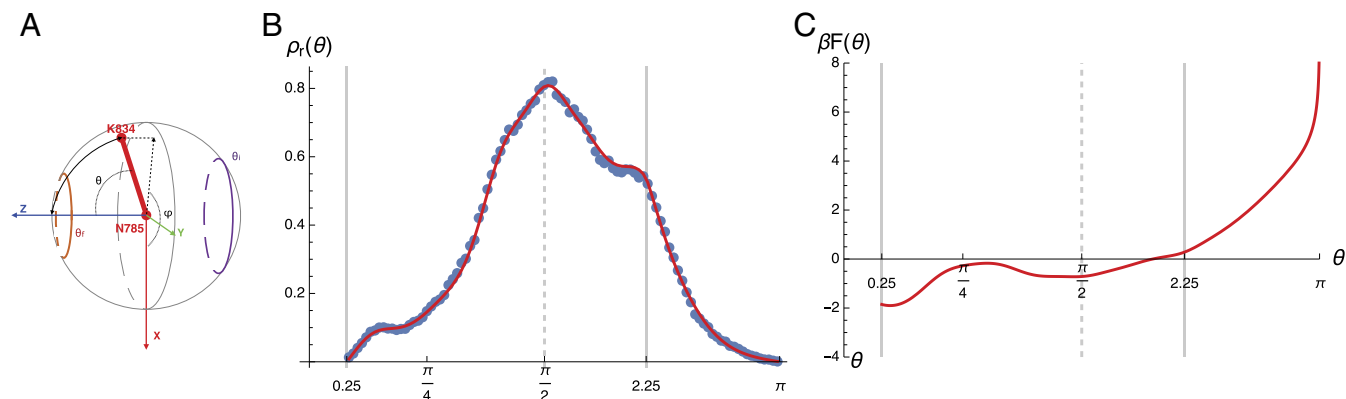


**Fig. 6.** Extraction of the potential driving the rotation. (A) Definition of the angles  $\theta$  and  $\phi$ . The Cartesian axes are shown in red, green, and blue. The direction of the lever arm is shown as a thick red line, with the position of N785 and K834 shown as spheres. Note from Fig. 2 B and C that the  $z$  axis is parallel to F-actin, so the  $\theta$  angle indicates the angle between the lever arm and the actin filament. The source and sink of the Fokker-Planck (FP) model are approximately shown in purple and orange, respectively. (B) The probability  $\rho_r(\theta)$ . The result from CG simulation is shown as blue solid circles. The fit of the data, obtained using *SI Appendix, Eq. S11*, is in red. The gray thick lines show the values of  $\theta_i = 2.25$  and  $\theta_f = 0.25$ . (C) The free energy obtained to fit  $\rho_r(\theta)$ . The gray thick lines are the same as in B.

This means that for a large part of the swing, the lever arm rotates stochastically while maintaining a hinge around N785. The capture toward the R state occurs only when the lever arm is sufficiently close to the motor domain. The stochasticity of the dynamics explains the large width in the distribution of  $\tau_{\chi 2} - \tau_{\chi 1}$ .

To extract the diffusion constant we compare the simulated mean first passage time (MFPT)  $\tau_r^{CG}(\theta)$  and the one resulting from a diffusing pseudoparticle in the potential  $F(\theta)$ . The theoretical MFPT is obtained by solving the one-dimensional FP equation using a constant diffusion coefficient (51),  $\tau_{FP}(\theta) = D^{-1} \int_{\theta_f}^{\theta} d\theta' e^{\beta F(\theta')} \int_{\theta'}^{\pi} d\theta'' e^{-\beta F(\theta'')}$ . Fitting  $D$  in  $\tau_{FP}(\theta)$  vs.  $\tau_r^{CG}(\theta)$  we obtain  $D \approx 0.011/\mu\text{s}$  (*SI Appendix, section 4*). The good agreement between  $\tau_{FP}(\theta)$  and  $\tau_r^{CG}(\theta)$  reported in *SI Appendix, Fig. S13* suggests that it is reasonable to assume that  $D$  is constant.

Although we derived a one-dimensional model that captures the features of the CG simulations, we stress that the rotation occurs on a sphere, which would be better captured by a 2D model. Indeed the azimuthal component might play an important role in the rotation of the lever arm.

**Comparison with Experiments.** We use our simulations to compare with experiments probing the stepping mechanism of MVI dimers (38). To follow the orientation of the lever arm during the stepping, the CaM bound to the IQ domain of MVI was labeled with a bifunctional rhodamine (BR) probe (38). The points of attachment are P66 and A73 and are shown in Fig. 2 B and C in black and gray, respectively. Sun et al. (38) inferred the rotational dynamics of the lever arm from the orientational changes in BR, using polarized total internal reflection fluorescence (polTIRF). This yielded the  $\theta$  angles (along the direction of actin, referred as  $\beta$  in ref. 38) and the  $\phi$  angle (the azimuthal angle is named  $\alpha$  in ref. 38). [Note that  $\theta$  and  $\phi$  are angles of the BR probe with respect to the reference system of actin (Fig. 2 B and C). In ref. 38, the Greek letters  $\theta$  and  $\phi$  are used to identify the angle of the lever arm in the reference system of actin, and  $\alpha$  and  $\beta$  are used for the probe. We compare here with  $\alpha$  and  $\beta$  of ref. 38]. The heads of the dimers in the leading and the trailing positions were identified, and the corresponding distributions of the  $\theta$  and  $\phi$  angles were extracted. According to kinetics experiments (52), both the trailing head (TH) and the leading head (LH) are in the ADP-bound state. In the TH, the lever arm swing has already occurred, and it is directed toward the pointed end of F-actin. In contrast, the LH, held under tension by the actin-bound TH, is in the uncoupled (U) state.

To compare our simulations with experiments, we reproduced the measurements by monitoring the orientation of the unit vec-

tor connecting A73 with P66 (Fig. 2 B and C). The  $\theta$  and  $\phi$  angles of the BR probe in the R-state crystal structure differ between the computational model ( $\theta_R^{CG}$  and  $\phi_R^{CG}$ ) and the values used in ref. 38 ( $\theta_R^{EXP}$  and  $\phi_R^{EXP}$ ). Two factors likely contribute to this discrepancy: (i) The alignment with F-actin and the choice of the reference system are not identical in experiments and simulations (our axes are rotated compared with those in ref. 38, so  $\phi \approx \alpha + \pi/2$ ), and (ii) we extracted the angles from the relative position of the  $\alpha$ -carbons of P66 and A73 from CaM, whereas experiments, in all likelihood, detect the orientation of the  $\beta$ -carbons (53).

To describe the TH, we consider the R-state conformations sampled in the simulations only at  $t > \tau_{\chi 3}$ , to ensure that the R state is reached. To sample the U state of the leading head, we ran 96 simulations of the swing of the lever arm by applying to the tip of the lever arm (K834) a backward load of 6 pN (details in *SI Appendix, section 1*), which mimics the effect of the inter-head tension. The mechanical force ( $f_L$ ) adopted to describe the U state resists the rotation of the lever arm by applying a momentum of the force of magnitude  $\approx r_{LA} f_L$ , where we consider a lever arm  $r_{LA} \approx 7.5$  nm (*SI Appendix, Fig. S10, Top*). If we consider the entire lever arm of MVI ( $r_{LA} \approx 18$  nm), the force that generates the same resistive momentum is  $f_L \approx 2.5$  pN, which is close to the upper bound of the interhead tension estimated experimentally [ $f_L \approx 2.2$  pN (16)]. This suggests that the magnitude of our backward load is not unrealistically high. We show in *SI Appendix, sections 2 and 3* that the backward load of 6 pN does not affect the first step of the PrePS  $\rightarrow$  R transition (*SI Appendix, Figs. S6–S8 and S20, SI Appendix, section 7, and Movies S5 and S6*), but it is sufficient to prevent the occurrence of the forward rotation of the lever arm in 95 of 96 cases (*SI Appendix, section 1 and SI Appendix, Fig. S3*). Thus, we generated the ensemble of U configurations as the collection of structures from the simulations conducted with a 6-pN backward load, sampling only the configurations for  $t > \tau_{\chi 1}$  for which the rotation of the lever arm was not completed.

Comparison of experimental data and simulations is provided in Fig. 7. We compared the following quantities reported in ref. 38: (i) the probability distribution for the LH and TH of the  $\theta$  angle (Fig. 7A), (ii) the probability distribution for the change in the  $\phi$  angle after one step ( $\Delta\phi$ , Fig. 7B), and (iii) and (iv) the probability distribution for the change after two steps of both the  $\theta$  angle (iii) ( ${}^2\Delta\theta$ , Fig. 7C) and the  $\phi$  angle (iv) ( ${}^2\Delta\phi$ , Fig. 7D). Because in experiments there is no control on the landing azimuthal angle of MVI on actin, the experimental distribution of the  $\phi$  angle for the LH and the TH is almost flat across  $180^\circ$ . In simulations, we always start from a MVI parallel to the  $x$  axis;

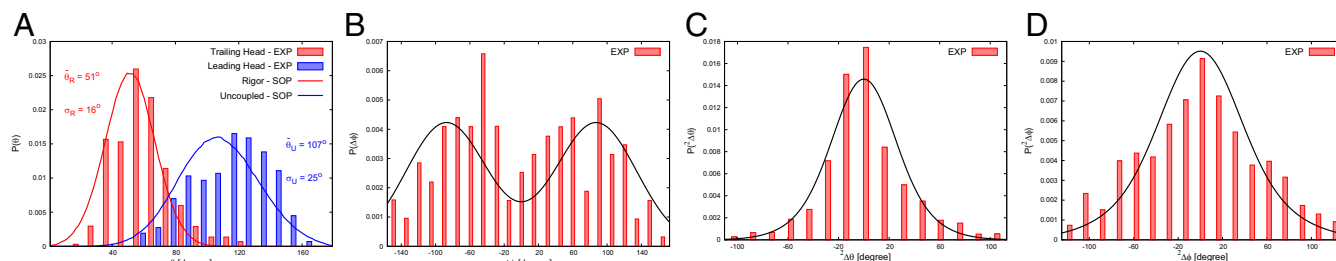


**Fig. 7.** Comparing simulations and experimental results. In A–D the histograms show the data extracted from figures 3 and 4 of ref. 38, whereas the lines show the results of our simulations and analyses. The red and blue lines are obtained directly from simulations and the black lines are from our model of a straight step of MVI dimer (*SI Appendix, section 5 and SI Appendix, Eqs. S17 and S18*), based upon the fit of the simulated distributions in A and in *SI Appendix, Fig. S15*. (A) Distribution of  $\theta$  ( $\beta$  in ref. 38) of the trailing (red) and leading (blue) heads. The data from simulations were fitted using normal distributions. The values of the means and dispersions are shown. The average of the distribution is denoted with a bar, and the SD is labeled as  $\sigma$ . (B) Distribution of the change of  $\phi$  after one step (*SI Appendix, Eq. S17*). (C) Distribution of the change of  $\theta$  after two steps (*SI Appendix, Eq. S18*). (D) Distribution of the change of  $\phi$  after two steps (*SI Appendix, Eq. S18*).

thus the comparison of calculated and measured distributions could be misleading (*SI Appendix, section 5* and *SI Appendix, Fig. S15*).

For comparison *i*, we extracted directly the probability distributions from the CG simulations of the U state and the R state to describe the LH and TH, respectively. We did not simulate consecutive steps. Thus, for comparisons *ii–iv* described above we created a simple model of the changes in the angles after one or two steps using two assumptions (details in *SI Appendix, section 5*): (*i*) The dimer always steps by a hand-over-hand mechanism, and (*ii*) the values of the angles after a step do not depend on the values before the step.

We found a remarkable agreement between the  $\theta$  angles obtained in simulation and experiment for both the LH and TH (Fig. 7*A*). Our CG model clearly reproduces the orientation and the fluctuations of the BR probe in the LH and TH, which validates the model. It should be stressed that we did not adjust any parameter in the CG model to obtain agreement with experiments.

Although the calculated changes in the  $\phi$  angle after one step agree with of the experimental data (Fig. 7*B*), there is a difference in the interpretation of the results based on simulations and experiments. According to experiments, in both the transitions LH $\rightarrow$ TH and TH $\rightarrow$ LH,  $\Delta\phi$  can be positive or negative with roughly equal probability (table 1 in ref. 38). From simulations we find that  $\Delta\phi$  is mostly ( $\approx 97\%$  of the time) positive (negative) in the R $\rightarrow$ U (U $\rightarrow$ R) transitions. Thus, in the simulations there is a contribution to each peak of  $P(\Delta\phi)$  from either R $\rightarrow$ U or U $\rightarrow$ R transitions, whereas in experiments each transition contributes to the two peaks almost equally. Furthermore, in our stepping model we assume that the direction of the interhead tension is always aligned with F-actin, which implies that only a 36-nm step occurs. But the measured broad step-size distribution in MVI suggests that this is not always the case.

Comparison of the probability distribution after two steps yields accurate results for the  $\theta$  angle (Fig. 7*C*), whereas our model for the distribution of  ${}^2\Delta\phi$  results in a somewhat more peaked distribution (Fig. 7*D*). This suggests that, in our model of stepping, MVI is not nearly as “wiggly” as inferred from experiments (38). A more quantitative comparison with experiments requires a CG model of MVI dimer in complex with F-actin.

## Discussion

**Position of the Hinge of the Rotatory Movement.** We suggest that the location of the hinge around which the lever arm rotates is close to residue N785 (located in ins2), at the beginning of a region identified as pliant in the PrePS state (41). Within a few microseconds from the start of the PrePS $\rightarrow$ R transition N785 binds the converter and then fluctuates around an average position (*SI Appendix, Figs. S9 and S18–S20*). Experiments have shown that chimeric constructs in which ins2 was truncated before (after) N785 and replaced with an artificial lever arm are plus-ended (minus-ended) motors (14, 54). Thus, from the structural viewpoint the location of the hinge is physically reasonable.

**The Uncoupling of the Lever Arm During the Power Stroke Is Intrinsic to the Motor Head.** The two-step PrePS $\rightarrow$ R transition with uncoupling of the lever arm at zero backward load suggests that it is not the presence of an actin-bound TH that induces the uncoupling of the lever arm. Our simulations illustrate that there is a possibility of a coupled swing to occur. However, this is unlikely at zero force and was observed only once when the 6-pN backward load was applied to the tip of the lever arm. Hence, the mechanism of uncoupling is inherent in the power stroke of MVI, and it is likely not due to gating or rearward tension. The flexibility of the LH lever arm was ascribed to the pliancy of the region between the lever arm and the converter (and perhaps the lever arm extension) (38) or to the uncoupling of the lever arm from the motor domain (30, 39, 41). In this paper we use “uncoupling”

because we observe that in the majority of the trajectories the rotation of the lever arm is not synchronous to the power stroke. On the other hand, we observe that part of ins2 (approximately up to N785) is tightly attached to the converter during the swing (*SI Appendix, Figs. S8, S18, and S20* and *Movies S1, S2, S5 and S6*), suggesting that the initial part of ins2 is not uncoupled from the motor domain. Thus, our simulations agree with the picture of a pliant lever arm around ins2.

**The Two-Step Mechanism.** It has been suggested that the power stroke of MVI occurs with a two-step mechanism, in which first the converter rotates, and then, once the backward load from the actin-bound trailing head is relieved, the lever arm rotates toward the R-state configuration (41). In this picture, it was argued that at the end of the first step the converter domain is in a PrePS state-like configuration, but it has moved toward the R-state position on the motor domain. We find that the converter domain not only translates and rotates to the R-state position on the motor domain (*SI Appendix, section 3* and *SI Appendix, Fig. S7*), but also assumes the conformation observed in the R-state crystal structure (the so-called R-fold of the converter; *SI Appendix, Figs. S7 and S8*). The flexibility around the hinge allows for these changes to occur even in the presence of a large backward load (*SI Appendix, Figs. S7 and S8* and *SI Appendix, section 3*). It is worth noting that we are not considering the effects of an azimuthal component of the backward load, which might add more complexity to the picture, as we suggested in comparing simulations and experimental results. Note that evidence from single-molecule experiments of MVI (8) and cryo-EM images of MV (55) suggests that the lever arm swing consists of two substeps: a large transition to the ADP-bound conformation triggered by Pi release and a smaller step occurring upon ADP release. Our two-step mechanism ignores the ADP-bound intermediate, and thus these two substeps suggested by experiments are incorporated into our second transition occurring between  $\tau_{\chi 2}$  and  $\tau_{\chi 3}$ . We cannot exclude that the converter domain occupies the P-fold conformation in the post-stroke state (41). We believe that a poststroke R-fold converter provides a more succinct picture of the MVI power stroke. Additional simulations and experiments are needed to resolve this subtle issue.

**The Lever Arm of MVI Rotates Stochastically, Preferentially on the Side of F-Actin.** Both the coupled and uncoupled trajectories suggest that the structure of the converter domain and the PrePS $\rightarrow$ R transition favor a rotation of the MVI lever arm on the side of the actin filament, that is, on the right side as seen by the observer in Fig. 2*B* and *C* (*Movies S1–S4* and *SI Appendix, Figs. S11, S12, S18, and S19*). As already pointed out in ref. 38, this might confer to MVI the experimentally observed right-handed twirling around the actin filament (20, 38). In the uncoupled simulations the rotation is stochastic: The azimuthal component of the lever arm undergoes large changes, and the flat free-energy landscape explored by the  $\theta$  component suggests that the rotational diffusion is almost free for a large part of the lever arm swing.

**The Connection Between the U State and the Occurrence of Short (Inchworm-Like) Steps.** A model was proposed to explain the presence of short inchworm-like steps in MVI motility (31). The authors suggest that a short step occurs if the free MVI head binds actin while the lever arm of the leading, actin-bound head is still in PrePS orientation. If the actin-bound MVI lever arm rotates to the R-state orientation, the dimer takes a long step. This scheme provides a structural picture that encompasses both the long and short steps of MVI, thus explaining the broad step-size distribution. Based on the two-step mechanism for the MVI power stroke, we propose that the short (inchworm-like) steps

occur if the TH rebinds F-actin before the rotation of the uncoupled lever arm, that is, before the completion of the second step of the PrePS→R transition. If the second step of the transition is completed, then the dimer takes a long step. Because ATP hydrolysis and the recovery stroke occur before the rebinding of the free head to F-actin, for our proposition to be valid the rotation of the uncoupled lever arm must occur on a timescale comparable to the rate of ATP hydrolysis, which was estimated to be  $\approx 10-17\text{ s}^{-1}$  (56). The timescale of transition from the U state to the R state is  $\langle \tau_{\chi 3} - \tau_{\chi 1} \rangle \approx 183\ \mu\text{s}$ , which is obtained for a lever arm of about 7.5 nm. The large steps of MVI dimers demand a combination of traditional lever arm and lever arm extension of roughly 36 nm for the dimer (ignoring the hinge between the two lever arms and the free myosin head). If we assume that the timescale of rotation scales with the length of the rotating rod as  $L^3/\ln(L/2a)$  (57), where  $a$  is the thickness of the rod (considering CaM it is  $\approx 3\text{ nm}$ ), the resulting timescale becomes about 2.5 ms, which is only  $\approx 20$  times faster than the highest bound for the measured rate of ATP hydrolysis. This suggests that it is plausible that the TH might bind before the lever arm of the leading head reaches the R state (that is, after  $\tau_{\chi 1}$ , but before  $\tau_{\chi 3}$ ).

**Uncoupling of the Lever Arm and Phosphate Release.** It is suggested that after the Pi is released and the power stroke is completed, the pathway for Pi escape closes, thus avoiding Pi rebinding and making the transition irreversible (2). Interestingly, a recent cryo-EM structure of MV bound to F-actin indicates that the nucleotide binding site in the poststroke, ADP-bound conformation cannot bind Pi even in the absence of backward load (55). Under high forces the power stroke of MV appears to be reversed (58). Because structural evidence suggests that the converter is mechanically coupled to the nucleotide binding site via the relay helix, the load-induced reversal of the power stroke would facilitate the recovery of a conformation of the motor domain capable of binding Pi and detaching more easily from F-actin, thus explaining the experimentally observed increase in the rate of detachment as a function of phosphate concentration (58).

The two-step model for the MVI power stroke suggests that at  $\tau_{\chi 1}$  the lever arm uncouples and the converter moves backward to the poststroke position. Thus, the backward load in MVI opposes the rotation of the converter back to the PrePS orientation instead of assisting it as in the case of MV (*SI Appendix, Fig. S16*). Hence, assuming that in MVI also only the prestroke conformation can bind Pi, we predict that, in contrast to MV, the detachment rate of MVI under load should not depend on the concentration of phosphate in solution.

**Predictions.** Our simulations lead to the following predictions: (i) As surmised elsewhere (41), the swing of the MVI lever arm occurs in two steps: first the converter reaches the R-state conformation while the lever arm points toward the barbed-end of F-actin and is uncoupled from the motor; subsequently the uncoupled lever arm rotates until it reaches the R-state conformation. The first step is only mildly dependent on backward load (*SI Appendix, Figs. S6–S8*). The uncoupling of the lever arm from the motor domain after the first step suggest that, in contrast to MV (58), the addition of Pi in solution should not lead to a faster detachment from F-actin of a backward-pulled MVI. (ii) The hinge around which the lever arm rotates is close to N785. (iii) The energetics of the lever arm during the rotation suggest that it is impeded to fully stretch backward. Furthermore, it is essentially uncoupled from  $\theta \approx 2.25\text{ rad}$  to  $\theta \approx \pi/4$  and only in the last part is captured by the motor domain. (iv) The swing of the MVI lever arm occurs primarily on the side of actin. (v) The typical time of rotation from the U state to the R state for a 7.5-nm lever arm is about 0.2 ms. This is consistent with a scheme in which short steps are taken whenever the trailing, free head

binds F-actin before the rotation of the uncoupled lever arm is completed, that is, before the second step of the PrePS→R transition.

## Conclusions

We studied the power stroke of MVI modeled as the transition from the PrePS state to the R state, focusing on the dynamics associated with the converter, ins2, and the IQ domain.

Our simulations allow us to draw two major conclusions: (i) The power stroke of MVI occurs in two steps. In the first step, the motor domain undergoes the PrePS→R transition, characterized by the movement of the converter, and then the lever arm rotates to the R-state conformation. (ii) During the rotation, the lever arm is largely uncoupled from the motor domain. The rotation of the lever arm is stochastic and occurs largely on the side of F-actin.

Our findings are based on a CG model of the PrePS→R transition in which (i) the side chains of the residues were not modeled, (ii) the Pi-release and ADP-bound structures of MVI were ignored, (iii) the role of F-actin (in the simulations carried out under backward load) is approximated with some tethering potentials restraining the external degrees of freedom of MVI, and (iv) the presence of a TH is modeled as a backward load of 6 pN directed parallel to F-actin. Although we believe that some of the restrictions could be relaxed in future studies, we do not expect our conclusions to be affected by a more comprehensive description of the MVI power stroke.

## Materials and Methods

**Preparation of the PrePS and R States.** We prepared the PrePS and R states by combining multiple PDB structures. The sequence and the two structures in Fig. 2 show that the model of MVI is made of the motor domain, the lever arm up to residue K834 of the IQ domain, and two bound CaMs.

The PrePS and R structures up to residue H786 (located in the middle of ins2; Fig. 2A) were taken from the PDB structures 4ANJ (41) and 2BKI (33), respectively. Because the distal parts of PDB structures 4ANJ and 2BKI were either partially substituted by GFP (4ANJ) or only partially solved (2BKI), we completed our model using the ins2, the IQ domain, and related CaMs of the PDB structure 3GN4 (23). To generate a continuous and seamless model, the residues 776–816 (a large part of ins2 and the beginning of the IQ domain; Fig. 2) of 4ANJ and 2BKI were superposed with the same residues in 3GN4, resulting in a rmsd of 0.38 Å and 0.47 Å, respectively. The resulting PrePS (R) structure in Fig. 2B (Fig. 2C) was used in our simulations.

Experiments (8, 59) suggest that the lever arm of MVI undergoes the following sequence of transitions: (i) From the ADP- and phosphate-bound PrePS state to a conformation in which the lever arm has not moved, but the motor domain is now primed for phosphate release (the PiR state) (59). (ii) Following the release of phosphate, the MVI head reaches an ADP-bound state. During this transition, most of the swing occurs, but the lever arm conformation does not correspond to the one in the R state (8) (see ref. 19 for a cryo-EM image). (iii) Following ADP release, the motor finally reaches the R state.

We set PrePS as the initial state and R as the final state, ignoring the intermediates that are either poorly structurally characterized (ADP bound) or close to our initial (PiR) or final (ADP-bound) states.

We did not model F-actin explicitly. Although binding to the track affects the way MVI proceeds through the cycle (5), we believe that it does not significantly affect our findings, because they depend on the conformational transition of the converter and only to a lesser degree on what triggers the movement of the converter. For the same reason, we presume that the absence of the intermediate states from our model will not impact significantly our conclusions.

**CG Model.** We created a CG representation of MVI, in which each amino acid is represented as a single bead centered at the  $C_{\alpha}$  position. We used the self-organized polymer (SOP) version of the CG model (60, 61), which is described in *SI Appendix, section 1*. Of relevance here is that the nature of the interaction between two beads depends on their distance in the native state. If their distance in the native state is below  $R_C = 8\text{ \AA}$ , and if they are at least three residues away from each other in the sequence, the two beads interact through an attractive potential of the Lennard–Jones type, with minimum at their native distance and well depth of  $\epsilon_{\text{NAT}} = 2\text{ kcal/mol}$ . The connectivity

of the chain is ensured by a finitely extensible nonlinear elastic potential between consecutive beads in the sequence. The interaction between all other pairs of beads is purely repulsive, with strength of the repulsion at the diameter of the beads  $\sigma = 3.8 \text{ \AA}$  equal to  $\epsilon_{\text{NNAT}} = 1 \text{ kcal/mol}$ .

**PrePS→R Transition.** To simulate the PrePS→R transition, we adopted the method in ref. 61 with minor variations, which were consistent with the results of fully atomistic molecular dynamics simulations of MVI carried out using the special-purpose Anton computer (*SI Appendix, Fig. S1*). This method (see *SI Appendix, section 1* for details) uses an energy function that simultaneously incorporates the native interactions in PrePS and in R states, and it mimics the effect of phosphate release by making the interactions associated with the PrePS state weaker, thus facilitating the PrePS→R transition.

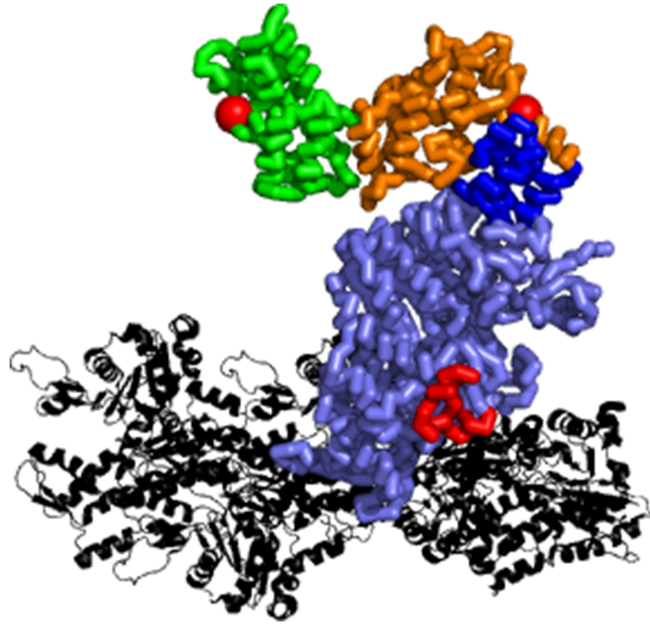
We generated 96 trajectories for long enough times to ensure that MVI has completed the PrePS→R transition. In these simulations we did not restrain the motor domain. Hence, the overall rotation of MVI was removed using the Kabsch algorithm (62, 63) to align the motor domain before the converter (residues 1–703, up to the end of the SH1 helix) to the motor domain of the R structure, which had been previously aligned to an actin-bound myosin II from PDB 1MVV. The rotation of the lever arm was monitored after carrying out this alignment. The converter domain and the lever arm, which are subject to the largest change, were not considered in the alignment.

- Geeves MA, Holmes KC (1999) Structural mechanism of muscle contraction. *Annu Rev Biochem* 68:687–728.
- Sweeney HL, Houdusse A (2010) Structural and functional insights into the myosin motor mechanism. *Annu Rev Biophys* 39:539–557.
- Buss F, Spudich G, Kendrick-Jones J (2004) Myosin VI: Cellular functions and motor properties. *Annu Rev Cell Dev Biol* 20:649–676.
- Frank DJ, Noguchi T, Miller KG (2004) Myosin VI: A structural role in actin organization important for protein and organelle localization and trafficking. *Curr Opin Cell Biol* 16:189–194.
- Pylpenko O, et al. (2015) Myosin VI deafness mutation prevents the initiation of processive runs on actin. *Proc Natl Acad Sci USA* 112:E1201–E1209.
- Yoshida H, et al. (2004) Lessons from border cell migration in the *Drosophila* ovary: A role for myosin VI in dissemination of human ovarian cancer. *Proc Natl Acad Sci USA* 101:8144–8149.
- Dunn TA, et al. (2006) A novel role of myosin VI in human prostate cancer. *Am J Pathol* 169:1843–1854.
- Lister I, et al. (2004) A monomeric myosin VI with a large working stroke. *EMBO J* 23:1729–1738.
- Rock RS, et al. (2001) Myosin VI is a processive motor with a large step size. *Proc Natl Acad Sci USA* 98:13655–13659.
- Nishikawa S, et al. (2002) Class VI myosin moves processively along actin filaments backward with large steps. *Biochem Biophys Res Commun* 290:311–317.
- Park H, et al. (2006) Full-length myosin VI dimerizes and moves processively along actin filaments upon monomer clustering. *Mol Cell* 21:331–336.
- Phichith D, et al. (2009) Cargo binding induces dimerization of myosin VI. *Proc Natl Acad Sci USA* 106:17320–17324.
- Yu C, et al. (2009) Myosin VI undergoes cargo-mediated dimerization. *Cell* 138:537–548.
- Elting MW, Bryant Z, Liao JC, Spudich JA (2011) Detailed tuning of structure and intramolecular communication are dispensable for processive motion of myosin VI. *Biophys J* 100:430–439.
- Jana B, Onuchic JN (2016) Strain mediated adaptation is key for myosin mechanochemistry: Discovering general rules for motor activity. *PLoS Comput Biol* 12:e1005035.
- Oguchi Y, et al. (2008) Load-dependent ADP binding to myosins V and VI: Implications for subunit coordination and function. *Proc Natl Acad Sci USA* 105:7714–7719.
- Sweeney HL, et al. (2007) How myosin VI coordinates its heads during processive movement. *EMBO J* 26:2682–2692.
- De La Cruz EM, Ostap EM, Sweeney HL (2001) Kinetic mechanism and regulation of myosin VI. *J Biol Chem* 276:32373–32381.
- Wells AL, et al. (1999) Myosin VI is an actin-based motor that moves backwards. *Nature* 401:505–508.
- Sun Y, Goldman YE (2011) Lever-arm mechanics of processive myosins. *Biophys J* 101:1–11.
- Rock RS, et al. (2005) A flexible domain is essential for the large step size and processivity of myosin VI. *Mol Cell* 17:603–609.
- Spink BJ, Sivaramakrishnan S, Lipfert J, Doniach S, Spudich JA (2008) Long single  $\alpha$ -helical tail domains bridge the gap between structure and function of myosin VI. *Nat Struct Mol Biol* 15:591–597.
- Mukherjee M, et al. (2009) Myosin VI dimerization triggers an unfolding of a three-helix bundle in order to extend its reach. *Mol Cell* 35:305–315.
- Kim H, Hsin J, Liu Y, Selvin PR, Schulten K (2010) Formation of salt bridges mediates internal dimerization of myosin VI medial tail domain. *Structure* 18:1443–1449.
- Thirumalai D, Zhang Z (2010) Myosin VI: How do charged tails exert control? *Structure* 18:1393–1394.
- Liu Y, Hsin J, Kim H, Selvin PR, Schulten K (2011) Extension of a three-helix bundle domain of myosin VI and key role of calmodulins. *Biophys J* 100:2964–2973.
- Mukherjee M, et al. (2014) Myosin VI must dimerize and deploy its unusual lever arm in order to perform its cellular roles. *Cell Rep* 8:1522–1532.
- Yildiz A, et al. (2003) Myosin V walks hand-over-hand: Single fluorophore imaging with 1.5-nm localization. *Science* 300:2061–2065.
- Ökten Z, Churchman LS, Rock RS, Spudich JA (2004) Myosin VI walks hand-over-hand along actin. *Nat Struct Mol Biol* 11:884–887.
- Yildiz A, et al. (2004) Myosin VI steps via a hand-over-hand mechanism with its lever arm undergoing fluctuations when attached to actin. *J Biol Chem* 279:37223–37226.
- Nishikawa S, et al. (2010) Switch between large hand-over-hand and small inchworm-like steps in myosin VI. *Cell* 142:879–888.
- Park H, et al. (2007) The unique insert at the end of the myosin VI motor is the sole determinant of directionality. *Proc Natl Acad Sci USA* 104:778–783.
- Ménétreay J, et al. (2005) The structure of the myosin VI motor reveals the mechanism of directionality reversal. *Nature* 435:779–785.
- Ménétreay J, Llinas P, Mukherjee M, Sweeney HL, Houdusse A (2007) The structural basis for the large powerstroke of myosin VI. *Cell* 131:300–308.
- Pylpenko O, et al. (2011) Role of insert-1 of myosin VI in modulating nucleotide affinity. *J Biol Chem* 286:11716–11723.
- Lan G, Sun SX (2006) Flexible light-chain and helical structure of f-actin explain the movement and step size of myosin-VI. *Biophys J* 91:4002–4013.
- Ikezaki K, Komori T, Arai Y, Yanagida T (2015) Lever arm extension of myosin VI is unnecessary for the adjacent binding state. *Biophys J* 11:47–53.
- Sun Y, et al. (2007) Myosin VI walks “wiggly” on actin with large and variable tilting. *Mol Cell* 28:954–964.
- Reifenberger JG, et al. (2009) Myosin VI undergoes a 180 power stroke implying an uncoupling of the front lever arm. *Proc Natl Acad Sci USA* 106:18255–18260.
- Ovchinnikov V, Cecchini M, Vanden-Eijnden E, Karplus M (2011) A conformational transition in the myosin VI converter contributes to the variable step size. *Biophys J* 101:2436–2444.
- Ménétreay J, et al. (2012) Processive steps in the reverse direction require uncoupling of the lead head lever arm of myosin VI. *Mol Cell* 48:75–86.
- Tozzini V (2005) Coarse-grained models for proteins. *Curr Opin Struct Biol* 15:144–150.
- Zhang Z, Thirumalai D (2012) Dissecting the kinematics of the kinesin step. *Structure* 20:628–640.
- Hyeon C, Thirumalai D (2011) Capturing the essence of folding and functions of biomolecules using coarse-grained models. *Nat Commun* 2:487.
- Whitford PC, Sanbonmatsu KY, Onuchic JN (2012) Biomolecular dynamics: Order-disorder transitions and energy landscapes. *Rep Prog Phys* 75:076601.
- Hyeon C, Onuchic JN (2007) Internal strain regulates the nucleotide binding site of the kinesin leading head. *Proc Natl Acad Sci USA* 104:2175–2180.
- Hyeon C, Onuchic JN (2007) Mechanical control of the directional stepping dynamics of the kinesin motor. *Proc Natl Acad Sci USA* 104:17382–17387.
- Chen LF, Winkler H, Reedy MK, Reedy MC, Taylor KA (2002) Molecular modeling of averaged rigor crossbridges from tomograms of insect flight muscle. *J Struct Biol* 138:92–104.
- Guo Z, Thirumalai D (1995) Kinetics of protein folding: Nucleation mechanism, time scales, and pathways. *Biopolymers* 36:83–102.
- Zhang Q, Bruijic J, Vanden-Eijnden E (2011) Reconstructing free energy profiles from nonequilibrium relaxation trajectories. *J Stat Phys* 144:344–366.
- Zwanzig R (2001) *Nonequilibrium Statistical Mechanics* (Oxford Univ Press, Oxford).
- Dunn AR, Chuan P, Bryant Z, Spudich JA (2010) Contribution of the myosin VI tail domain to processive stepping and intramolecular tension sensing. *Proc Natl Acad Sci USA* 107:7746–7750.



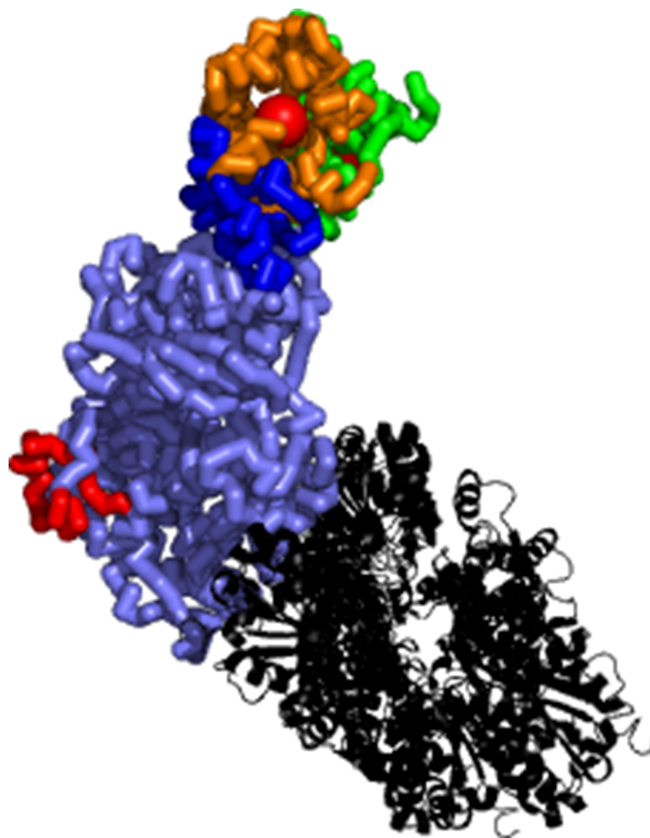
# Supporting Information

Mugnai and Thirumalai 10.1073/pnas.1615708114



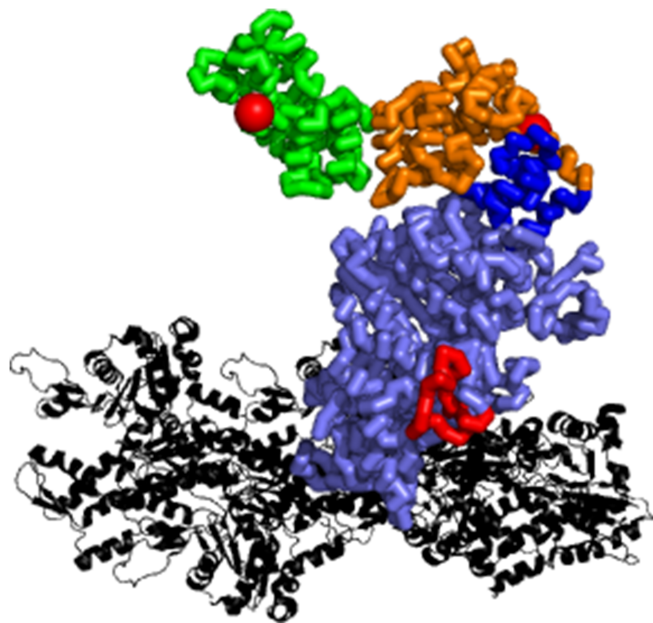
**Movie S1.** The PreP5→R transition for an uncoupled trajectory in the absence of load. The observer is on the side of the actomyosin complex. The myosin is colored as in Fig. 2 of the main text. The residues N785 and K834 are shown as red spheres, and their size is exaggerated for visibility. F-actin is shown for reference. The total duration is about 55  $\mu$ s.

[Movie S1](#)



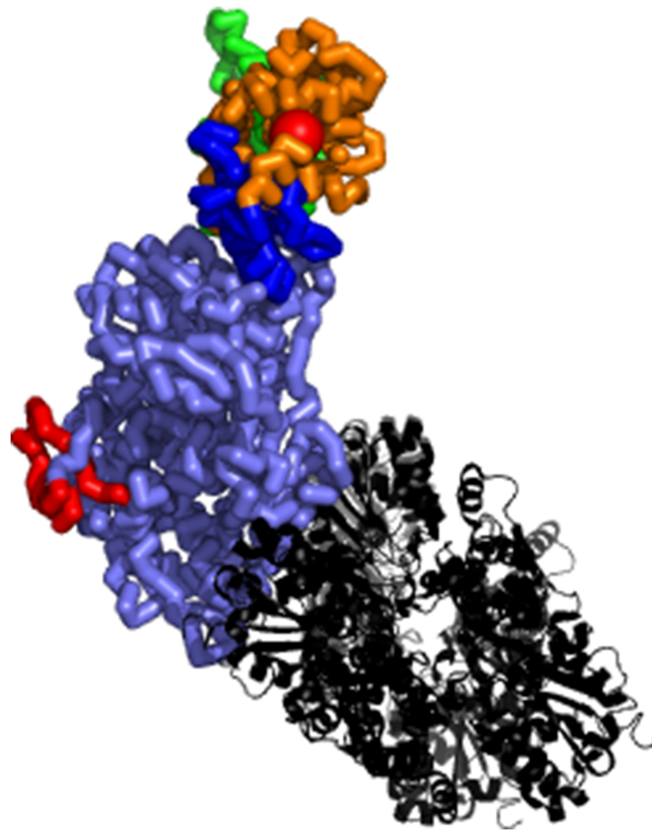
**Movie S2.** The PrePS→R transition for an uncoupled trajectory in the absence of load. The observer is on F-actin, behind the myosin looking toward the minus end of the filament. The myosin is colored as in Fig. 2 of the main text. The residues N785 and K834 are shown as red spheres, and their size is exaggerated for visibility. The actin filament is shown for reference. The total duration is about 55  $\mu$ s.

[Movie S2](#)



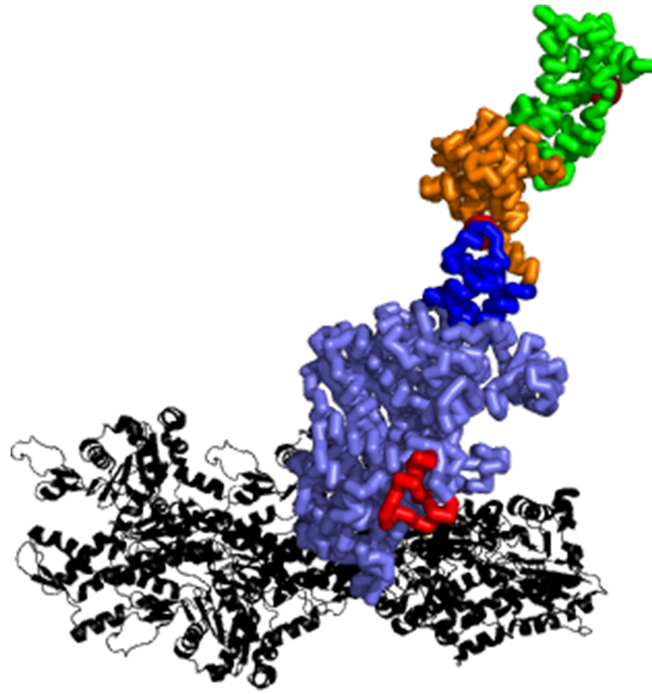
**Movie S3.** The PrePS→R transition for a coupled trajectory in the absence of load. The observer is on the side of the actomyosin complex. The myosin is colored as in Fig. 2 of the main text. The residues N785 and K834 are shown as red spheres, and their size is exaggerated for visibility. F-actin is shown for reference. The total duration is about 55  $\mu$ s.

[Movie S3](#)



**Movie S4.** The PreP5→R transition for a coupled trajectory in the absence of load. The observer is on F-actin, behind the myosin looking toward the minus end of the filament. The myosin is colored as in Fig. 2 of the main text. The residues N785 and K834 are shown as red spheres, and their size is exaggerated for visibility. F-actin is shown for reference. The total duration is about 55  $\mu$ s.

[Movie S4](#)



**Movie S5.** The PrePS→R transition under 6 pN restive load for an uncoupled trajectory. The observer is on the side of the actomyosin complex. The myosin is colored as in Fig. 2 of the main text. The residues N785 and K834 are shown as red spheres, and their size is exaggerated for visibility. F-actin is shown for reference. The total duration is about 55  $\mu$ s.

[Movie S5](#)



**Movie S6.** The PrePS $\rightarrow$ R transition under 6 pN resistive load for an uncoupled trajectory. The observer is on F-actin, behind the myosin looking toward the minus end of the filament. The myosin is colored as in Fig. 2 of the main text. The residues N785 and K834 are shown as red spheres, and their size is exaggerated for visibility. The F-actin filament is shown for reference. The total duration is about 55  $\mu$ s.

[Movie S6](#)

## Other Supporting Information Files

[SI Appendix \(PDF\)](#)

# Supplementary Information

## Kinematics of the Lever Arm Swing in Myosin VI

M. L. Mugnai<sup>1,2,\*</sup>, D. Thirumalai<sup>1,2,\*</sup>

<sup>1</sup> *Biophysics Program, Institute for Physical Science and Technology, University of Maryland, College Park, MD 20742*

<sup>2</sup> *Department of Chemistry and Biochemistry, University of Maryland, College Park, MD 20742*

\* *Current address: Department of Chemistry, The University of Texas at Austin, Austin, TX 78712*

## Contents

<b>1</b>	<b>Coarse-grained method</b>	<b>3</b>
1.1	Self-Organized Polymer (SOP) energy function. . . . .	3
1.2	Conformational transition between two states. . . . .	4
1.3	Comparison with atomically-detailed simulations. . . . .	5

1.4	Constant resistive-force simulations. . . . .	6
1.5	Integration of the equation of motion. . . . .	7
1.6	Physical timescales. . . . .	7
1.7	Length of simulations. . . . .	8
1.8	Modeling the structures. . . . .	8
1.9	Dependence of the results on the model. . . . .	9
<b>2</b>	<b>The PrePS→R transition of the motor domain before the converter.</b>	<b>11</b>
<b>3</b>	<b>The rotation of the converter at around <math>\tau_{\chi 1}</math>.</b>	<b>11</b>
<b>4</b>	<b>The rotation of Ins2 and IQ after <math>\tau_{\chi 1}</math> in the coupled and uncoupled trajectories</b>	<b>13</b>
4.1	Coupled trajectories. . . . .	14
4.2	The free energy of the lever arm swing for uncoupled trajectories. . . . .	14
4.3	Mean first passage time of the uncoupled trajectories. . . . .	16
4.4	Convergence of the simulations. . . . .	16
<b>5</b>	<b>Comparison with experimental data.</b>	<b>17</b>
5.1	Probability distribution of angles in leading and trailing head. . . . .	17
5.2	Stepping model. . . . .	17
<b>6</b>	<b>The Movement of the Converter in MVI is Assisted by the Load.</b>	<b>18</b>
<b>7</b>	<b>Movies</b>	<b>19</b>

# 1 Coarse-grained method

**1.1 Self-Organized Polymer (SOP) energy function.** We used the coarse-grained (CG) Self-Organized Polymer (SOP) model of myosin VI (MVI) [1, 2], in which solvent, cosolvent, and the ligands (ADP and phosphate) are taken into account implicitly. Each amino acid is represented as one bead positioned at the  $C_\alpha$  of the residue. The beads interact according to a potential that depends on the structure of the protein in the native state. In terms of  $r_{i,j}$ , the distance between beads  $i$  and  $j$ , the SOP energy function is,

$$H(\vec{r}_1, \dots, \vec{r}_N | X) = \sum_{i=1}^{N-1} U_{\text{FENE}}(r_{i,i+1}) + \sum_{i=1}^{N-2} U_{\text{NNAT}}(r_{i,i+2}) + \quad (\text{S1})$$

$$\sum_{i=1}^{N-3} \sum_{j=i+3}^N U_{\text{NAT}}(r_{i,j} | X) \Theta(R_C - r_{i,j}(X)) + \sum_{i=1}^{N-3} \sum_{j=i+3}^N U_{\text{NNAT}}(r_{i,j} | X) [1 - \Theta(R_C - r_{i,j}(X))].$$

The first term in Eq. S1, enforcing connectivity of the chain, is the finitely-extensible non-linear elastic (FENE) potential given by,

$$U_{\text{FENE}}(r_{i,i+1}) = -\frac{1}{2} k_F R_F^2 \log \left[ 1 - \frac{(r_{i,i+1} - r_{i,i+1}^0)^2}{R_F^2} \right], \quad (\text{S2})$$

where  $k_F$  is the stiffness of the interaction, and  $R_F$  is the upper bound of the displacement allowed from the native distance. The equilibrium distance  $r_{i,i+1}^0$  between two consecutive beads is either fixed at  $3.8\text{\AA}$  or extracted from the crystal structure (nearly  $3.8\text{\AA}$ ).

The second term in Eq. S1 involves beads that are separated by two residues from each other in the sequence. This term enforces the geometry of the next nearest neighbor beads, so that they do not overlap. The functional form is a purely repulsive, short range potential,

$$U_{\text{NNAT}}(r_{i,j}) = \epsilon_{\text{NNAT}} \left( \frac{\sigma}{r_{i,j}} \right)^6, \quad (\text{S3})$$

with energy scale  $\epsilon_{\text{NNAT}}$ , and range  $\sigma$  for all beads.

The third term in Eq. S1 describes interactions between two beads  $i$  and  $j$  with  $|i - j| > 2$  that are within a distance  $R_C$  in the native structure of the  $X$  state, i.e.  $r_{i,j}(X) < R_C$ . The

form of the potential is,

$$U_{\text{NAT}}(r_{i,j}) = \epsilon_{\text{NAT}} \left[ \left( \frac{r_{i,j}(X)}{r_{i,j}} \right)^{12} - 2 \left( \frac{r_{i,j}(X)}{r_{i,j}} \right)^6 \right], \quad (\text{S4})$$

with the minimum energy  $-\epsilon_{\text{NAT}}$  at  $r_{i,j}(X)$ , the distance between the two  $\text{C}_\alpha$  atoms in the crystal structure.

The last term in Eq. S1 is a purely repulsive potential (Eq. S3) between  $i$  and  $j$  ( $|i-j| > 2$ ) beads with the distance in the native structure  $r_{ij}(X) > R_C$ . We also use the same form of the potential to describe interactions between two beads  $i$  and  $j$  ( $|i-j| > 2$ ) where at least one of the two residues is not resolved in the X-ray structure, and was added to maintain connectivity of near-neighbor residues.

The model depends on six parameters, listed in Table S1, that have been used previously to reveal GroEL and myosin V dynamics [1, 2]. Of the six parameters,  $\sigma$ ,  $k_F$ , and  $R_F$  (Table S1) are not relevant, in the sense that results are unlikely to change as long as their values are physically reasonable. Thus, the SOP energy function has only three relevant parameters, which, as stated above, are the same as in previous studies, attesting to the transferability of the SOP model for investigating the dynamics in large molecular complexes.

The neglect of side chains, which we were forced to do for computational reasons, might seem to be a drastic approximation as it excludes sequence-specific interactions. However, the excellent agreement between simulations and experiments, without adjusting any parameter, validates the model. Previously, we showed that similar models were effective in providing nearly quantitative description of the stepping kinetics of kinesin [3].

**1.2 Conformational transition between two states.** To allow for transitions between multiple states we modified the SOP potential to encode both the native contacts of the initial and the final states simultaneously in the energy function. To accomplish this goal, we adopted a variant of a strategy used to study the rigor to post-rigor transition in myosin V [2].

We divide all the pairs of residues  $i$  and  $j$  (with  $|i-j| > 2$ ) into four sets: if the two beads

are in contact both in the PrePS and R state native structure, the pair belongs to the set  $\mathcal{N}_{\text{PrePS} \cap \text{R}}$ ; the set  $\mathcal{N}_{\text{PrePS}}$  ( $\mathcal{N}_{\text{R}}$ ) constitutes the pairs of beads that are in contact in PrePS (R) but not in R (PrePS); if the beads are not in contact either in PrePS nor in R state, they belong to  $\mathcal{N}_{\text{NAT}}$ . The method proposed in [2] is the following. If the pair belongs to  $\mathcal{N}_{\text{PrePS}}$  ( $\mathcal{N}_{\text{R}}$ ), we use Eq. S4, with the minimum at the native distance for the PrePS (R). For the pairs of beads in  $\mathcal{N}_{\text{NAT}}$ , we use Eq. S3. If the pair belongs to  $\mathcal{N}_{\text{PrePS} \cap \text{R}}$ , the potential embodies information about both the initial and the final structure. We adopt for the PrePS $\rightarrow$ R transition the functional form used in [2] for the rigor to post-rigor transition,

$$U_{\text{SWITCH}}(r_{ij}) = \min \left( \alpha U_{\text{NAT}}(r_{ij} | \text{PrePS}), U_{\text{NAT}}(r_{ij} | \text{R}) \right). \quad (\text{S5})$$

The  $\alpha$  parameter in Eq. S5 skews the potential in favor of the ending state, thus facilitating the transition between the two states. We used essentially the same scheme in this study with a modification. We found by generating a few trajectories that the lever arm swing did not occur using Eq. S5. More importantly, the structure of MVI was distorted. By using the following potential for interaction between beads in  $\mathcal{N}_{\text{PrePS}}$ ,

$$U_{\text{NAT}}(r_{i,j} | \text{PrePS}) = \alpha_{\epsilon \text{NAT}} \left[ \left( \frac{r_{ij}(\text{PrePS})}{r_{ij}} \right)^{12} - 2 \left( \frac{r_{ij}(\text{PrePS})}{r_{ij}} \right)^6 \right], \quad (\text{S6})$$

we found that the aforementioned problem was solved. This modification yielded the results described in the main text. Following [2], we used  $\alpha = 0.5$ . We show below that other choices of  $\alpha$  do not give results that are in agreement with experiments.

To speed up the calculation, we precomputed the crossing point  $\zeta$  between the two potentials in Eq. S5. We adopted only a one minimum potential if the crossing point was at zero, at infinity (practically at  $\zeta > 100r_{ij}(X)$ ), or did not exist.

**1.3 Comparison with atomically-detailed simulations.** To establish that using the potential in Eq. S6 is physically reasonable, we show the time trace of the distance between G121 (in the motor domain) and A764 (in the converter) for the MVI power stroke simulation in SOP model carried out with and without the modification presented in Eq. S6 (see Fig. S1). We compare these results with the time trace of the G121-A764 distance from fully-atomistic

simulations carried out using the resources made available through Anton, a supercomputer capable of performing extremely fast molecular dynamics simulations [4]. We ran multiple microsecond-long fully-atomistic simulations starting from the phosphate-release structure (PiR) [5], with the phosphate in the binding pocket slightly rotated, which likely enhances the chances of seeing its escape. In the PiR state, the converter domain is nearly the same as in the PrePS state. Comparison of the fully-atomistic and SOP simulations is shown in Fig. S1. The red (blue) trajectory shows G121-A764 distance in a SOP model of the PrePS→R transition with (without) the modification in Eq. S6 of the method in [2]. The green and purple lines are obtained from fully-atomistic trajectories, and they show that in less than a microsecond the G121-A764 contact is broken. In MD simulations the contact reforms because the converter does not reach the R-state conformation in microsecond time scale. This does not occur in CG simulations because the converter rapidly rotates to the post-stroke conformation. Nevertheless, the comparison in Fig. S1 shows that the weak interaction between the converter and motor domain is captured only if the PrePS contacts that are not formed in R are described using Eq. S4 scaled by the parameter  $\alpha$ , as in Eq. S6.

**1.4 Constant resistive-force simulations.** In the simulations in which we pulled the lever arm backward with a constant resistive force ( $F_E$ ), we used a tethering potential to ensure that  $F_E$  does not induce an overall rotation and translation of the protein. The external force was applied to the last bead of the lever arm, K834 (see Fig.2b-c), resulting in a potential,

$$U_{\text{PULL}}(r_{\text{K834}}) = -\vec{F}_E \cdot (\vec{r}_{\text{K834}} - \vec{r}_{\text{K834}}(X)), \quad (\text{S7})$$

where  $\vec{r}_{\text{K834}}(X)$  is the position of K834 in state  $X$ . To tether the protein to the initial position, we restrained with a harmonic spring the geometric centers of four sets of beads (V394-K408, I525-N533, Q541-K550, and K632-L638) to their position in the R state. The tethering potential applied to each one of these groups is,

$$U_{\text{TETHER}} = \frac{1}{2}k_{\text{TETHER}} \left( \vec{R}_{\text{CM}} - \vec{R}_{\text{CM}}(X) \right)^2, \quad (\text{S8})$$

where  $\vec{R}_{\text{CM}}$  is the current position of the center of mass of the group, and  $\vec{R}_{\text{CM}}(X)$  is the position in state  $X$ . The constant  $k_{\text{TETHER}}$  was set to  $1\text{kcal}/(\text{mol}\text{\AA}^2)$ .

**1.5 Integration of the equation of motion.** We modeled the dynamics of MVI using Brownian dynamics and integrated the equations of motion using the algorithm [6],

$$x_i(n+1) = x_i(n) + \frac{F_i(n)}{\xi} dt + \sqrt{2\frac{k_B T}{\xi}} dt \mathcal{R}_i(n), \quad (\text{S9})$$

where  $i$  is the bead index,  $n$  refers to the integration step,  $\xi$  is the friction,  $k_B$  is the Boltzmann constant,  $T$  is the temperature, and  $\mathcal{R}_i(n)$  is a random process with mean zero, and variance  $\langle \mathcal{R}_i(n) \mathcal{R}_j(n') \rangle = \delta_{n,n'} \delta_{i,j}$ , with  $\langle \dots \rangle$  meaning an average over the noise, and  $\delta_{i,j}$  is the Kronecker symbol. To integrate successfully the fastest frequency in the model, which is due to the FENE potential, we used  $dt/\xi = 5.779 \cdot 10^{-3} \text{\AA}^2/(\text{kcal/mol})$ . This is a conservative upper bound, obtained by trial and error. For much larger values of  $dt/\xi$  the FENE interactions were found to diverge. The non-native interactions between beads  $i$  and  $j$  (see Eq. S3) were truncated at  $3\sigma$ . To speed up the calculations, we implemented a neighbor list with buffer of  $0.3\text{nm}$ . For the majority of the simulations, the list was updated dynamically every time that the sum of the displacements of the two beads that moved the most from the previous update exceeded  $0.3\text{nm}$ . In comparing with MD simulations, we updated the lists every 10 steps. Although this scheme is in principle less accurate, the resulting distributions of the direction of the lever arm, of  $\tau_{\chi 1}$ ,  $\tau_{\chi 2}$ , and  $\tau_{\chi 3}$ , and other quantities that we monitored did not show significant differences from those obtained using the more accurate method.

**1.6 Physical timescales.** To get the correct time scale for our simulations, we would need an accurate estimate of the friction coefficient in Eq. S9, which includes the contribution from all the degrees of freedom that our model ignores. This is difficult to carry out, thus we rely on the following argument: we observe that the long-range dynamics is dominated by the attractive Lennard-Jones interactions, which bring the largest (by a factor  $\approx 10$ ) contribution to the energy of the system. The interactions are of the form  $u(r) = \epsilon f(\sigma_N/r)$ , which introduces a typical length scale  $\sigma_N$ , and a typical energy scale  $\epsilon$ . The energy scale is the

same for all the pairs of interacting beads, while the typical length depends on the native contact distance. We then take the average of those native-contact distances in the Rigor or PrePS states as the length scale:  $\sigma_N = 6.3\text{\AA}$ . To get the typical timescale of the simulation, we rewrite the Brownian equation in reduced units [7], indicated with a superscript “\*”. If we use as typical units for temperature  $\epsilon/k_B$ , and for the random noise  $\sqrt{\tau^{-1}}$ , where  $\tau$  is the typical time, we get,

$$\xi\dot{x} = F + \sqrt{2k_B T \xi} R \rightarrow \frac{\xi\sigma_N}{\tau}\dot{x}^* = \frac{\epsilon}{\sigma_N}F^* + \sqrt{2T^* \frac{\epsilon\xi}{\tau}}R^* \rightarrow \dot{x}^* = \frac{\epsilon\tau}{\xi\sigma_N^2}F^* + \sqrt{2T^* \frac{\epsilon\tau}{\xi\sigma_N^2}}R^*.$$

The natural choice for the time scale of the simulation is  $\tau = \frac{\xi\sigma_N^2}{\epsilon}$ . Now, using the Stokes’ formula for the friction ( $\xi = 3\pi\eta\sigma_N$ , where  $\eta$  is the dynamic viscosity of water) and plugging in the numbers we obtain,

$$\tau = \frac{\xi\sigma_N^2}{\epsilon} \approx 92\text{ps}, \quad (\text{S10})$$

which is close to (although somewhat smaller than) previous estimates made for protein folding [8] and SOP models [1, 2].

**1.7 Length of simulations.** For the simulations of the PrePS→R transition at zero load, the equations of motion were integrated at least until  $\tau_{\chi_3}$  (see Fig. 3a) is reached. This occurred typically within  $10^8$  steps (368  $\mu\text{s}$ ), but in some cases a longer integration time was necessary (around 1.9 times longer). For the simulations of the PrePS→R transition with backward load, we carried out  $10^8$  time steps for each trajectory (details in the SI section “**Comparison with experimental data**”).

**1.8 Modeling the structures.** The PrePS and R structures were obtained by combining experimentally resolved structures, as described in the main text. Since some residues were missing in the experimental structures, we bridged the gaps by adding the beads corresponding to the the missing residues to maintain the connectivity of the chain. Such beads were allowed to have only bonded and purely repulsive interactions. To model them, they

were initially placed on a straight line connecting the last residue solved before the gap, and the first residue solved after the gap. A sequence of short simulations and minimizations using a conjugate-gradient algorithm [9] were used to find a good initial structure for the sequence. To avoid distortions in the protein, the beads corresponding to residues that were experimentally solved were tethered at their crystallographic position.

**1.9 Dependence of the results on the model.** As explained before, the SOP model has only three relevant parameters, (i) the strength of the native interactions,  $\epsilon_{\text{NAT}}$ , (ii) the strength of the non-native interactions,  $\epsilon_{\text{NNAT}}$ , and (iii) the cutoff distance for native interactions,  $R_C$ . To describe the PrePS $\rightarrow$ R transition, we introduce a fourth parameter (iv)  $\alpha$ , which penalizes the PrePS native contacts, as was done in [2]. We ask the following questions: (A) how do our results depend on these parameter choices? (B) Is our choice of parameters justifiable? The strength of the interactions and the cutoff range might affect the dynamics of the lever arm, thus altering the free energy profile  $F(\theta)$  (Fig. 6c). On the other hand, as explained in the section “**Comparison with experimental data**” in the main text, we find that with a backward load comparable with the experimentally estimated maximum force exerted by the actin-bound trailing head on the leading head [10] the lever arm swing is arrested. (Only one out of the 96 trajectories under load completed the transition during the duration of the simulation, and we found that trajectory to be coupled.) Intuitively, stronger R-state native interactions with the lever arm might drive the rotation forward at higher backward loads, while a lower backward load might be enough to impede the rotation if the native interactions are weaker. Furthermore, the good agreement between the simulated and experimental [11] distributions of  $\theta$  angle of the probe orientation (Fig. 7a) suggests that the flexibility of the lever arm is captured by the SOP model. These considerations justify the choice of the SOP energy function parameters. In addition, the excellent agreement between SOP simulations and experiments, with the same parameters as those used in many different examples, further shows that minimal energy scales can describe the dynamics of molecular machines.

The weakening of the PrePS interactions mimics, a priori, the effect of phosphate release, which leads to the power stroke. Thus, we expect the “correct” strength of the switching potential to be  $0 < \alpha < 1$ , but we do not know the exact value. To explore the effect of the intensity of the switching parameter on the PrePS→R transition, we carried out 96 simulations at  $\alpha = 0.6, 0.7, 0.8$  both with and without a 6pN backward load. We ran each of these 576 simulations for  $10^8$  steps ( $368\mu s$ ), and counted the number of completed runs (that is, simulations in which the second transition in  $\chi$  was observed) as a function of load and  $\alpha$ . As shown in Fig. S2, both the number of completed simulations in the presence and in the absence of load increases as a function of  $\alpha$ . The 6pN resistive force is still able to interrupt (or slow down) the PrePS→R transition in a large number of runs. We then analyzed the trajectories, and computed the number of coupled and uncoupled PrePS→R transitions observed (Fig. S3). Regardless of the backward load, increase in  $\alpha$  results in an increase in the number of coupled trajectories. We used this qualitative difference between simulations carried out at different values of the switching parameter to deduce the most appropriate value of  $\alpha$ . As a measure of the quality of the simulations, we compared the distribution of angles between the bifunctional rhodamine (BR) probe and F-actin for the leading head, which was experimentally determined in [11]. In Fig. S4 we show that those trajectories that are completed despite the presence of a backward load are by and large the coupled ones - only in one case (for  $\alpha = 0.7$ ) was an uncoupled trajectory under load completed. Strikingly, while for  $\alpha < 0.8$  all the coupled trajectories reach the R conformation regardless of the load applied, for  $\alpha = 0.8$  a force of 6pN successfully interrupts (or slows down) the swing in a large number of trajectories. Thus, we compare with experiments the following distributions of angle between the BR probe and F-actin: the distribution resulting from (i) uncoupled and (ii) coupled trajectories in which the PrePS→R transition was not completed, and (iii) coupled trajectories in which the PrePS→R transition was completed. The comparisons in Figs. S5 clearly show that only the arrested uncoupled trajectories reproduced the experimental data, thus suggesting that coupled lever arm swings

might take place - if at all - very rarely. Hence, we found that an appropriate choice of the  $\alpha$  parameter is the one that minimizes the occurrence of coupled runs, and we adopted  $\alpha = 0.5$ , in agreement with the previous study on myosin V [2].

## 2 The PrePS $\rightarrow$ R transition of the motor domain before the converter.

Let the motor domain be the residues 1-703 of MVI, that is from the N-terminus to the SH1 helix, before the converter. During the first transition of the structural overlap function, the motor domain undergoes a structural transition from PrePS to R. To visualize the transition, we show in Fig. S6  $\Delta\text{RMSD}(t) = \langle \text{RMSD}(\text{R}) - \text{RMSD}(\text{PrePS}) \rangle(t)$ , where  $\text{RMSD}(\text{R})$  ( $\text{RMSD}(\text{PrePS})$ ) is the root-mean-square deviation from the R (PrePS) conformation, and  $\langle \dots \rangle(t)$  indicates the average over the trajectories at time  $t$ . When the structure is close to the PrePS conformation (for  $t \approx 0$ ),  $\Delta\text{RMSD}(t) > 0$ . At  $t \approx \tau_{\chi 1}$  the negative value of  $\Delta\text{RMSD}(t)$  indicates that the transition to the R conformation of the motor domain is completed. Thus, in our model, the transition from the PrePS to the R conformation of the motor domain occurs rapidly (for  $t < \tau_{\chi 1}$ ).

## 3 The rotation of the converter at around $\tau_{\chi 1}$ .

During the first step of MVI power stroke, the converter domain moves from the PrePS position (on the -end side of MVI motor domain), to the R position (on the +end side of MVI motor domain). This movement can be characterized as a rigid body translation of  $\approx 1.9\text{nm}$  approximately in the  $-\hat{z}$  direction, and a rigid body rotation of  $\approx 104^\circ$  approximately around  $\hat{x}$  (see Figs. 2b-c for the axes). Furthermore, the conformation of the converter changes from the P-fold, populated in the PrePS state (a unique feature of MVI [12]), to the R-fold, which is instead found in the R state ( $\text{RMSD} \approx 3.4\text{\AA}$ ). In a former two-step model for the MVI swing [13] it was suggested that the first step of the power stroke consists of the movement

of the converter to the post-stroke position while maintaining the P-fold. We show here that our model differs from the picture suggested in [13], because after  $\tau_{\chi_1}$  we found that the converter populates preferentially the R-fold, and it occupies the post-stroke orientation.

We devised three functions that allow us to monitor the displacement, rotation, and structural change of the converter at  $t = \tau_{\chi_1}$ , and we report the average over the 94 uncoupled trajectories of these quantities as a function of time. First, we monitored the geometric center of the converter after aligning the trajectory to a R-state MVI aligned to F-actin (see “**Materials and Methods**” in the main text). In Fig. S7c we show the average position of the geometric center with and without backward load. At around  $\tau_{\chi_1}$  the converter is translating to the post-stroke position and remains there until the end of the simulation. (Note that in the presence of the backward load the converter undergoes a displacement in the direction of the force larger than in the simulations carried out without load.)

To investigate the rotation of the converter we monitor the difference in the  $\theta$  angle (the angle with respect to  $\hat{z}$ , i.e. F-actin) between two vectors: the first is  $\vec{r}_R$ , connecting N477 to Y721 (red in Figs. S7a-b), and the second,  $\vec{r}_G$ , connects N477 to C754 (green in Figs. S7a-b). Let the difference between these two angles be  $\delta\theta = \arccos(\vec{r}_R \cdot \hat{z}/|r_R|) - \arccos(\vec{r}_G \cdot \hat{z}/|r_G|)$ . From Figs. S7a-b, we observe that  $\delta\theta$  is negative in PrePS state, and positive in R. In Figs. S7d, we show the results of the uncoupled trajectories obtained with and without the 6pN backward load. At the beginning of the simulation the difference  $\delta\theta$  is negative, and it crosses zero at  $t \approx \tau_{\chi_1}$ . For  $t > \tau_{\chi_1}$ , the average of  $\delta\theta$  shows that the converter is close to the orientation observed in the R state.

We also monitored the conformation of the converter by measuring the structural overlap function (Eq. 1) of the converter alone (residues 706-773) with respect to the converter in P-fold ( $\chi_{\text{PrePS}}$ ) and in R-fold ( $\chi_{\text{R}}$ ). We used as a scoring function  $(\chi_{\text{PrePS}} - \chi_{\text{R}})/|\chi_{\text{PrePS}} - \chi_{\text{R}}|$ , which is -1 if the converter is closer to the P-fold, and +1 if it is closer to the R-fold. From Fig. S7e it is clear that even before  $\tau_{\chi_1}$  the converter tends to be in the R-fold. As a further evidence that the converter is in the R-state conformation after  $\tau_{\chi_1}$ , we monitored the

probability density function (PDF) of the distance  $\Delta$  between the residues A741 and V781 after  $\tau_{\chi 1}$  in simulations carried out with and without backward load. The contact between these beads is formed exclusively in the R-fold (see Fig. S8a-b). We compared the resulting distribution with the PDF for the same distance monitored during a set of 32 simulations of the PrePS state (that is, SOP model without the switching potential) of 147.2  $\mu$ s each. From Fig. S8c we deduce that, regardless of the backward load, after  $\tau_{\chi 1}$  the converter forms this R-fold contact, which is not formed in the P-fold.

We conclude that at around  $\tau_{\chi 1}$  the converter has not only translated, but also rotated towards the R-state configuration and has undergone a conformational transition to the R-fold. The presence of a 6pN-backward load does not affect these findings.

## 4 The rotation of Ins2 and IQ after $\tau_{\chi 1}$ in the coupled and uncoupled trajectories

To follow the movement of the lever arm in space, we monitor the relative position of N785 and K834, whose locations in the PrePS and in R state are shown in Fig. 2b-c as red spheres. A sample trajectory in Fig. S9 shows the change in the location of N785 and K834 during the PrePS $\rightarrow$ R transition. The trajectory is color-coded red for  $t \leq \tau_{\chi 1}$ , green for  $\tau_{\chi 1} < t \leq \tau_{\chi 2}$ , blue for  $\tau_{\chi 2} < t \leq \tau_{\chi 3}$ , and black for  $t > \tau_{\chi 3}$ . During the initial stage of the transition, the position of N785 changes significantly (red part of the trajectory). Subsequently, it fluctuates but maintains its average position. In contrast, after the initial relaxation, K834 shows a large movement (green part of the trajectory) that ends in a configuration close to the R state (black). To dissect the movements further, we monitor the relative position of N785 and K834 in spherical coordinates. The resulting time trace of the spherical coordinates for a specific trajectory is reported in Fig. S10. The distance  $R_{NK}$  between N785 and K834 does not drift significantly. The  $\theta$  angle is close to  $5\pi/6$  in PrePS and it jumps to  $\approx 0$  in R. The  $\phi$  angle starts around  $\pi$ , and when  $\theta$  reaches its value in the R state, it fluctuates over

entire the range  $[0, 2\pi]$ . Because the distance  $R_{\text{NK}}$  is roughly constant during the transition, the lever arm rotation occurs as a rigid rotation with major changes only in  $\theta$  and  $\phi$ . In Fig. S11 we show MVI aligned to F-actin in PrePS and in the R conformation. The black points represent a sample of the position in space of K834 during the PrePS $\rightarrow$ R transition in the 94 uncoupled trajectories, and the continuous lines connect the position of K834 during 5 different trajectories. We draw the following conclusions: (i) the trajectories are stochastic, (ii) the azimuthal angle changes during the swing (see for instance green and magenta trajectories), (iii) the lever arm rotates preferentially on the side of F-actin - that is, on the right hemisphere from the perspective of the observer represented as an eye.

**4.1 Coupled trajectories.** Since we have only two coupled trajectories they can be easily visualized in a single plot, as in Fig. S12, which shows that: (i) the two trajectories are different, (ii) the swing appears to be rapid, which is consistent with a lever arm coupled to the converter, (iii) both the trajectories occur mostly in the right hemisphere as seen from the perspective of the observer represented as an eye. We also made a movie of a coupled trajectory seen from a side (Movie3) and from behind (Movie4) (see also SI section “**Movies**”).

**4.2 The free energy of the lever arm swing for uncoupled trajectories.** Although the rotation of the lever arm occurs on a 2D spherical surface, as a first approximation we use as a 1D reaction coordinate the angle  $\theta$ , describing the projection of the lever arm on  $\hat{z}$ , which is parallel to F-actin. We generate a stationary probability distribution on the unit circle,  $\rho_r(\theta)$ , by using the procedure described in [14]. We define a source at  $\theta_i$ , from which the trajectories are injected, and an absorbing state at  $\theta_f$ , at which the trajectories are terminated and removed (see Fig. 6a). A stationary flux is obtained if the amount of trajectories injected balances exactly those removed through the absorbing state. We achieve this stationary flux state by combining the trajectories in the following way. The first trajectory starts from  $\theta_i$  at  $t = 0$  and it reaches  $\theta_f$  at a certain time  $\tau_1$ . Suddenly, the system jumps back to  $\theta_i$ , where the second trajectory starts at  $t = \tau_1$ . The second trajectory

ends when it crosses  $\theta_f$  at a time  $\tau_1 + \tau_2$ , and so on. We extract the segment of each trajectory  $\nu$  of the  $N_U = 94$  uncoupled trajectories, adopting  $\theta_i = 2.25\text{rad}$  ( $\approx 129^\circ$ ), close to the PrePS state ( $\theta_{\text{PrePS}} \approx 2.55\text{rad}$ ), and  $\theta_f = 0.25\text{rad}$  ( $\approx 14.3^\circ$ ), close to the R state ( $\theta_R \approx 0.04\text{rad}$ ). In order to construct the stationary probability distribution  $\rho_r(\theta)$  we divide the domain  $[\theta_f, \pi]$  in 100 identical bins and compute the probability density function per bin. Following the procedure highlighted in [14], and assuming a constant diffusion coefficient we connect the non-equilibrium, stationary probability distribution  $\rho_r(\theta)$  to the free energy  $F(\theta)$  governing the rotation on the lever arm along  $\theta$ :

$$\rho_r(\theta) = \begin{cases} Q^{-1} e^{-\beta F(\theta)} \int_{\theta_f}^{\theta} d\theta' e^{\beta F(\theta')} & \theta \leq \theta_i \\ Q^{-1} e^{-\beta F(\theta)} \int_{\theta_f}^{\theta_i} d\theta' e^{\beta F(\theta')} & \theta > \theta_i \end{cases} \quad (\text{S11})$$

where  $Q$  is the partition function. To extract  $F(\theta)$ , we approximated it as the sum of  $N_g$  Gaussians and a term reminiscent of the underlying Jacobian:

$$\beta F(\theta) = \sum_{i=1}^{N_g} a_i e^{-\frac{(x-\mu_i)^2}{2\sigma_i^2}} - \log(\sin(\theta)). \quad (\text{S12})$$

We fixed the value of the center of two gaussians to be the extreme  $\theta$  angles, 0 and  $\pi$ . We then added Gaussians close to the maxima (minima) of  $\rho_r(\theta)$ , and set the sign of the  $a_i$  coefficients to be negative (positive). We adjusted by trial and error all the parameters to minimize the difference between the simulated probability distribution (Fig. 6b), and the probability distribution obtained with Eq. S11. We found by trial and error that  $N_g = 8$  was sufficient to reproduce the simulated probability distribution in Fig. 6b. This requires knowledge of 22 parameters that were first guessed by trial and error, then refined using an automated fitting procedure implemented in Mathematica [15], in which a distance is defined between the 100 points sampled from the CG simulations ( $\rho_r^{\text{CG}}(\theta)$ ) and the 100 estimated points ( $\rho_r(\theta|\vec{p})$ ) for the function  $\rho_r(\theta)$ ,

$$\Xi(\vec{p}(n)) = \sum_{i=1}^{100} \left( \rho_r^{\text{CG}}(\theta_i) - \rho_r(\theta|\vec{p}(n)) \right)^2, \quad (\text{S13})$$

where  $\vec{p}(n)$  is the vector indicating the 22 free parameters at the  $n$ -th step of the optimization. We then updated each parameter following a simple steepest descent minimization scheme for 30 steps of fixed amplitude 0.0001. The resulting parameters are provided in Table S2.

**4.3 Mean first passage time of the uncoupled trajectories.** We extracted the mean first passage time (MFPT) from the CG simulations ( $\tau_r^{CG}(\theta)$ ) using the same segments of trajectories used to construct  $\rho_r(\theta)$ . We divided the set  $[\theta_f, \pi]$  into 10 bins, and for each conformation  $i$  we found the bin to which it belonged and we extracted  $\Delta t_\nu(i) = T_\nu - t_\nu(i)$ , that is the difference between the time for termination of the trajectory  $\nu$  ( $T_\nu$ ) and the time at which the bin was visited ( $t_\nu(i)$ ). We then averaged  $\Delta T_\nu(i)$  over all the conformations sampled, and over all the 94 uncoupled trajectories observed. To test the accuracy of a constant rotational diffusion coefficient we compared  $\tau_r^{CG}(\theta)$  with the MFPT of a pseudo-particle subject to a potential  $F(\theta)$  and a constant diffusion coefficient  $D$  by solving [16],

$$D e^{\beta F(\theta)} \frac{d}{d\theta} \left[ e^{-\beta F(\theta)} \frac{d}{d\theta} \tau_{\text{FP}}(\theta) \right] = -1. \quad (\text{S14})$$

By imposing an absorbing boundary at  $\theta_f$  ( $=0.25\text{rad}$ ) and a reflective boundary at  $\pi$ , we integrate Eq. S14 twice and find the solution [16],

$$D \tau_{\text{FP}}(\theta) = \int_{\theta_f}^{\theta} d\theta' e^{\beta F(\theta')} \int_{\theta'}^{\pi} d\theta'' e^{-\beta F(\theta'')}. \quad (\text{S15})$$

We solved the integrals in Eq. S15 numerically for 100 values of  $\theta \in [\theta_f, 2\pi]$ , and fit the resulting points to a eighth-order polynomial, which yields  $D \tau_{\text{FP}}(\theta)$ . We then fit the diffusion constant  $D$  in  $\tau_{\text{FP}}(\theta)$  versus  $\tau_r^{CG}(\theta)$  obtained from the coarse-grained simulations. The result, shown in Fig. S13, indicates that a constant diffusion coefficient is adequate for a one-dimensional model of the lever arm swing. The fit yields  $D \approx 0.011/\mu\text{s}$ .

**4.4 Convergence of the simulations.** In this section we discuss whether our sample of 94 uncoupled trajectories is sufficient to obtain a converged probability distribution  $\rho_r(\theta)$ . In Fig. S14, we show the probability distribution  $\rho_r(\theta)$  at different values of the angle  $\theta$  (identified by the color) as a function of the number of trajectories considered to extract

the probability distribution. After approximately 80 trajectories, at almost all  $\theta$ -values the distribution is constant, and further sampling does not significantly change the value of  $\rho_r(\theta)$ . This suggests that our estimate of the stationary probability distribution in  $\theta$  has reached convergence.

## 5 Comparison with experimental data.

**5.1 Probability distribution of angles in leading and trailing head.** To compare our results with the distributions for the changes in  $\theta$  and  $\phi$  angles measured in experiments [11], we need to extract from our simulations  $P(\Delta\gamma)$  and  $P(^2\Delta\gamma)$ , which are the probability distributions for the changes in the angle  $\gamma$  after one and two steps, respectively. Since we did not simulate consecutive steps, we obtained the changes in the angles by extracting the information from the distributions of the  $\theta$  and  $\phi$  angles in the pre-stroke (uncoupled, U) and post-stroke (R) state, which are meant to mimic the leading head (LH), and trailing head (TH) of the dimer, respectively. The distribution of the angles in the U and R state are fit to normal distributions  $\mathcal{N}(\bar{\gamma}, \sigma)$ , where  $\bar{\gamma}$  is the first moment of the Gaussian, and  $\sigma^2$  is the variance. Thus, we get  $P_R(\gamma) = \mathcal{N}(\bar{\gamma}_R, \sigma_R)$  and  $P_U(\gamma) = \mathcal{N}(\bar{\gamma}_U, \sigma_U)$ , where the fit and the parameters for  $\theta$  are in Fig. 7a, and those related to the angle  $\phi$  are in Fig. S15. Note that, as we already discussed in the main text, the agreement with experiments in the distribution of  $\theta$ -angles is very good, but the simulated distributions for the  $\phi$ -angle are more peaked than those observed in experiments. However, we use the data from the fitting of the computed distributions to extract the probability distribution for the changes of the angle  $\phi$  after one or two steps.

**5.2 Stepping model.** To derive the probability distribution of changes in the angles after one or two steps, we make two assumptions: (1) we assume that the value of an angle after the step is independent of the value of the angle before the step, and (2) we assume that the stepping occurs by a hand-over-hand mechanism. From the first assumption, we get that the

probability of change of the angle  $\gamma$  after a  $X \rightarrow Y$  transition equal to,

$$P_{X \rightarrow Y}(\Delta\gamma) = \mathcal{N}(\bar{\gamma}_Y - \bar{\gamma}_X, \sqrt{\sigma_X^2 + \sigma_Y^2}). \quad (\text{S16})$$

The second assumption implies that, after a step, a LH (TH) becomes a TH (LH), allowing us to consider only the following one-step transitions, LH $\rightarrow$ TH and TH $\rightarrow$ LH. Similarly, after two steps a LH (TH) head returns to a leading (trailing) position, so the transitions after two steps are LH $\rightarrow$ LH and TH $\rightarrow$ TH. Thus, for one step we get that the change in the angle  $\gamma$  is distributed according to,

$$P(\Delta\gamma) = 0.5[P_{R \rightarrow U}(\Delta\gamma) + P_{U \rightarrow R}(\Delta\gamma)]. \quad (\text{S17})$$

Similarly, the probability distribution of the change in the angle  $\gamma$  after two steps is,

$$P(^2\Delta\gamma) = 0.5[P_{R \rightarrow R}(\Delta\gamma) + P_{U \rightarrow U}(\Delta\gamma)]. \quad (\text{S18})$$

## 6 The Movement of the Converter in MVI is Assisted by the Load.

In [17] it was shown that a strong backward load on MV can invert the lever arm swing and induces detachment from actin with a phosphate concentration-dependent rate. As we explain in the main text, in the pre-stroke conformation Pi can escape from MV nucleotide binding site, but it cannot rebind in the post-stroke conformation (recent cryo-EM images suggest that the post-stroke motor domain is not able to bind phosphate [18]). Because in MV the backward load assists the return of the converter from the post-stroke to the pre-stroke conformation (Fig. S16, top panel), the phosphate concentration-dependent rate of detachment results from the re-opening of the Pi-release pathway induced by the backward load. According to our simulations, during the first step of the PrePS $\rightarrow$ R transition MVI reaches the uncoupled conformation, in which the motor domain is in the post-stroke conformation. During this transition, the converter domain moves in the same direction as the converter of MV; it is the presence of ins2 which reverses the gear of the motor, that is the

orientation of the lever arm. Hence, the backward load opposes the return of the converter to the pre-stroke conformation (Fig. S16, bottom panel). Assuming that, similarly to MV, the nucleotide binding site of MVI is able to bind Pi only in pre-stroke conformation, we suggest that MVI rate of detachment under load will not be affected by the phosphate concentration.

## 7 Movies

We made six movies to illustrate the PrePS→R transition of an uncoupled (Movie1 and Movie2) and a coupled trajectory (Movie3 and Movie4) in the absence of backward load. Movie5 and Movie6 show two uncoupled trajectories obtained with a 6pN-force directed as  $-\hat{z}$  applied to the tip of the lever arm. The color code in the movies is the same as in Fig. 2. The size of the beads corresponding to residues N785 (the hinge or the lever arm rotation) and K834 (the last residue of our MVI model) is exaggerated for visibility. F-actin is shown for reference, it was not part of the simulation. The total length of the movies is  $\approx 55\mu\text{s}$ , the time interval between two frames is  $\approx 0.22\mu\text{s}$ . Movie1, Movie3 and Movie5 are shown from a side, and Movie2, Movie4, and Movie6 are shown from behind MVI. From Movie1 and Movie5, it is clear that in an uncoupled trajectory the movement of the converter precedes the rotation of the lever arm. The coupled trajectory in Movie3 shows that in this case the rotation of the lever arm is faster, and almost simultaneous to the movement of the converter. Movie2 and Movie4 illustrate that the lever arm undergoes a swing on the side of F-actin. Furthermore, the 6pN backward load (Movie5 and Movie6) prevents the swing of the lever arm, but does not affect the rotation of the converter.

Finally, in Fig. S18-S20 we show a few still images from the movies, but seen from above MVI to better highlight the movements. Fig. S18 shows a sequence of conformational changes during an uncoupled swing of the lever arm. Fig. S18a is close to the initial conformation, in Fig. S18b-c ins2 is directed forward, and the converter assumes the post-stroke position. The last three panels show the lever arm swing (Fig. S18d-f). Note that N785, shown as a red sphere in ins2 (orange), does not move significantly after the initial rotation of the

converter. An example of coupled rotation of the lever arm is reported in Fig. S19. The six panels are taken over a much shorter time than the six in Fig. S18 (see the captions to the figures). Note that the lever arm swing is already underway while N785 is still moving towards the position that it occupies in the R-state conformation. Finally, in Fig. S20 we show an uncoupled trajectory under load. The time frames are the same as in Fig. S18. As in Fig. S18, after panel c N785 does not move significantly, but, in contrast to the rotation in the absence of load, the swing of the lever arm is arrested.

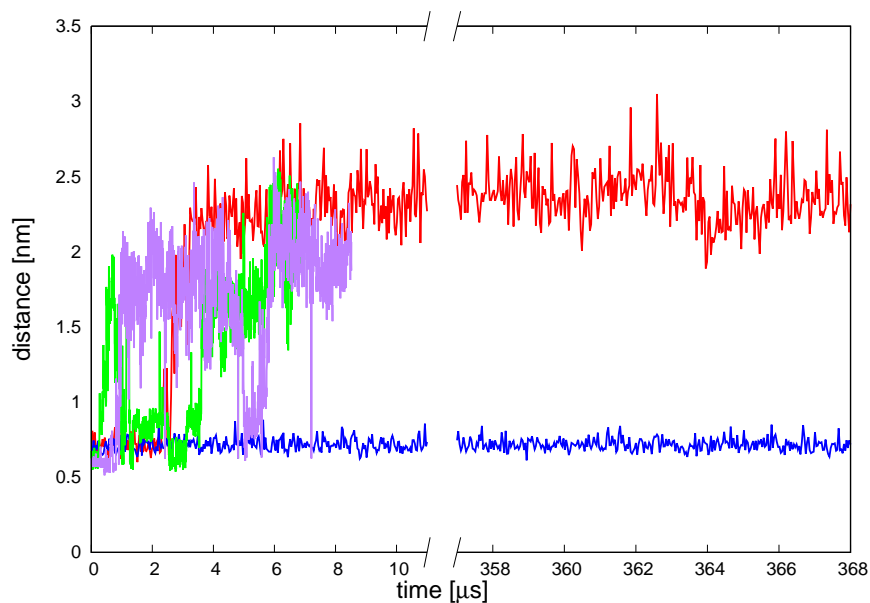


Figure S1: Time traces of the distance between G121 and A764 in four simulations. Red: SOP simulation of the PrePS→R transition with the double-well potential scheme modified for this study (Eq. S5 and Eq. S6). Blue: SOP simulations of the PrePS→R transition with the original double-well potential scheme (Eq. S5) [2]. Green and Purple: two fully-atomistic trajectories started from the phosphate-release structure. The trends found in CG simulations using Eq. S6 (red) are consistent with those found in all-atom simulations (green and purple).

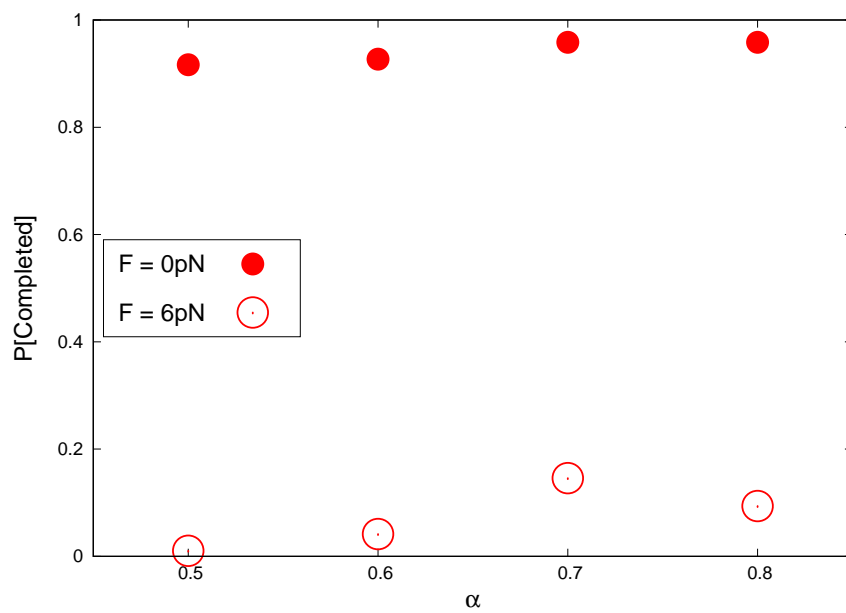


Figure S2: Probability of completing the PrePS→R swing as a function of  $\alpha$ . Full symbols: probability that the PrePS→R swing is completed within  $368\mu\text{s}$  ( $P(\text{completed})$ ) in the absence of backward load. The effect of backward load is shown by the empty symbols, which report  $P(\text{completed})$  as a function of  $\alpha$  when  $F=6\text{pN}$ .

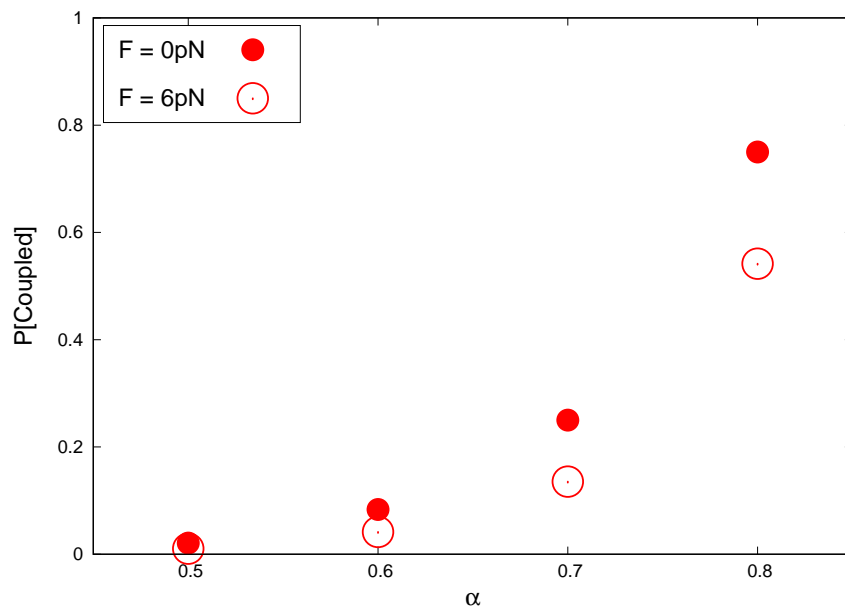


Figure S3: Probability of coupled trajectories as a function of  $\alpha$ . Full symbols: probability of generating a coupled PrePS $\rightarrow$ R swing ( $P(\text{coupled})$ ) in the absence of backward load. The effect of backward load is shown by the empty symbols, which report  $P(\text{coupled})$  as a function of  $\alpha$  when  $F=6\text{pN}$ .

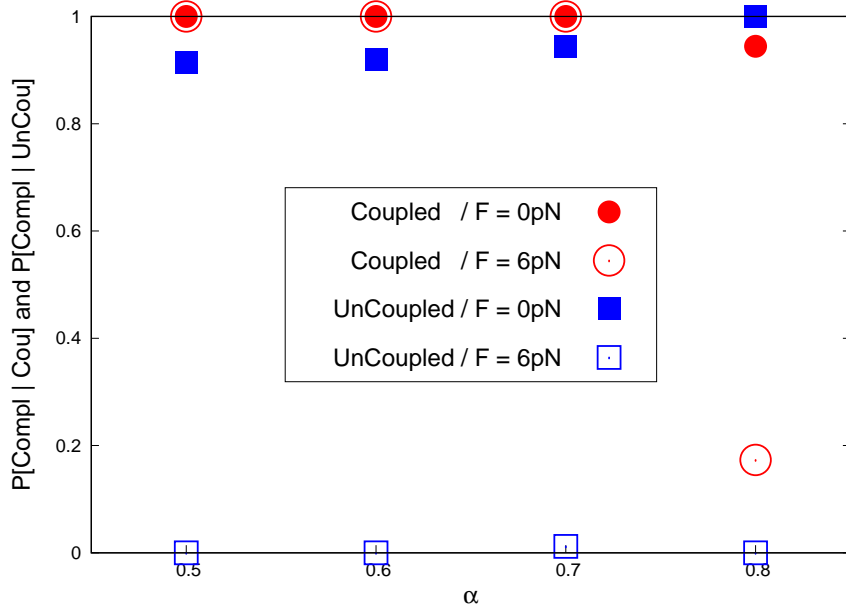


Figure S4: Probability of completing the PrePS $\rightarrow$ R transition as a function of  $\alpha$  for coupled and uncoupled trajectories. Full symbols: probability of completing the PrePS $\rightarrow$ R transition within  $368\mu\text{s}$  upon observing a coupled trajectory ( $P(\text{completed}|\text{coupled})$ , in red) or uncoupled ( $P(\text{completed}|\text{uncoupled})$ , in blue) in the absence of backward load. The effect of backward load is shown by the empty symbols, which report in red  $P(\text{completed}|\text{coupled})$  and in blue  $P(\text{completed}|\text{uncoupled})$  as a function of  $\alpha$  when  $F=6\text{pN}$ .

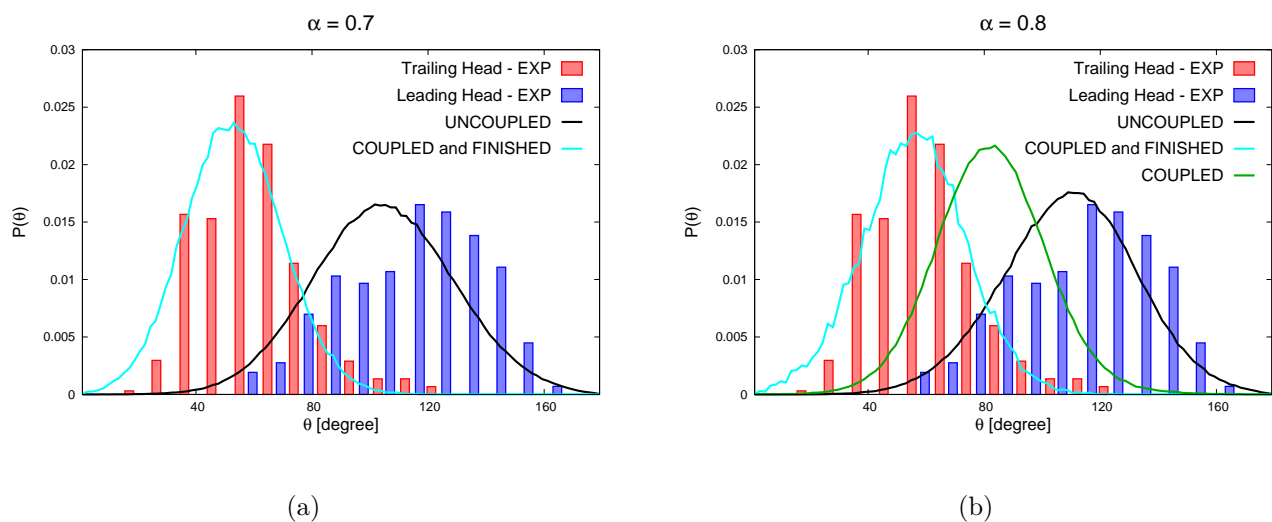


Figure S5: Comparison between experiments [11] and simulations with  $\alpha = 0.7$  and  $\alpha = 0.8$ . The figure shows the distribution of the angle between the bifunctional rhodamine probe (attached to a calmodulin) and F-actin. The histograms show the experimental distribution from [11] for the leading (LH, blue) and trailing (TH, red) head. The cyan continuous line is the distribution obtained considering exclusively the coupled simulations that reached the R conformation and for  $t > t_{\chi 3}$ . The distribution for uncoupled trajectories is reported as a black, continuous line. The green continuous line is the distribution obtained considering exclusively the coupled simulations that did not finish the run in  $368\mu\text{s}$ . Note that the angular distributions for the coupled and finished trajectories (cyan) are close to the experimental distribution for the TH. The results for the coupled trajectories arrested by the backward load (green) fall in between the LH and TH experimental distributions, without matching either. Thus, only the uncoupled runs that were arrested by backward load provide a good description of the conformation of the LH in a MVI dimer. Panel (a) shows the case in which  $\alpha = 0.7$ , the results obtained with  $\alpha = 0.8$  are reported in panel (b).

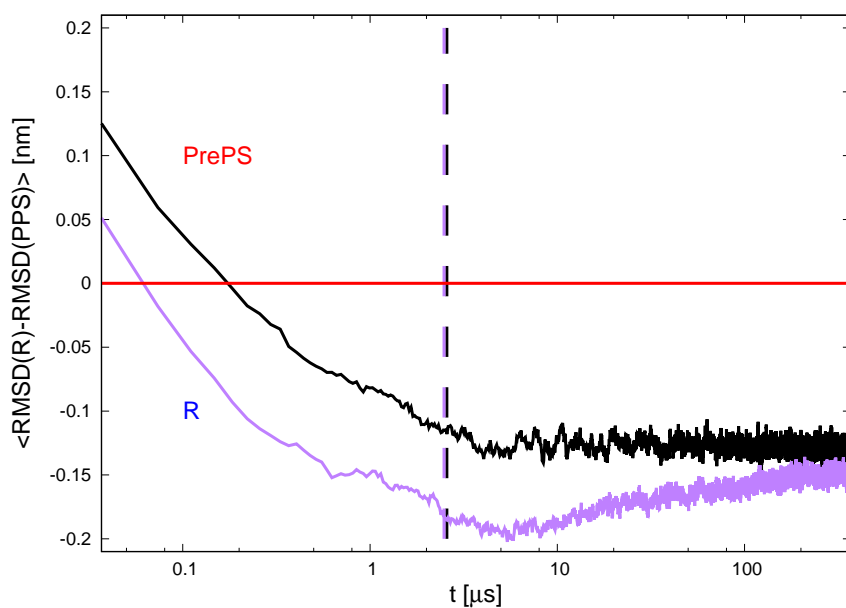
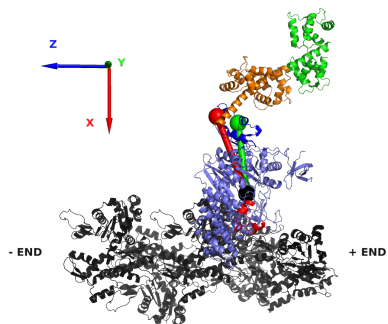
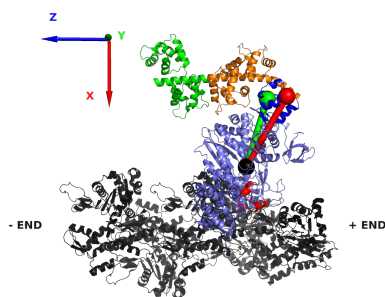


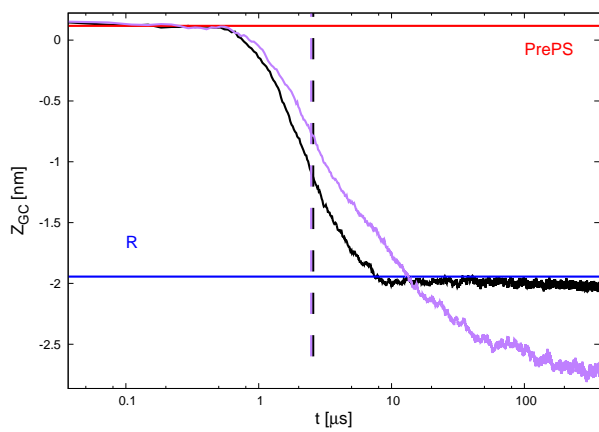
Figure S6: Transition dynamics by the motor domain monitored using the root-mean-square deviation (RMSD) measure. The continuous lines show the average over the trajectories of the difference of the RMSD with the R conformation and with the PrePS conformation. A positive (negative) value of this difference indicates that the structure is closer to the PrePS (R) conformation. The RMSD was calculated with respect to residues 1-703, representing the motor domain excluding the converter. The dashed vertical lines indicate  $\tau_{\chi 1}$ . The black (purple) lines refer to simulations ran in the absence (presence) of backward load.



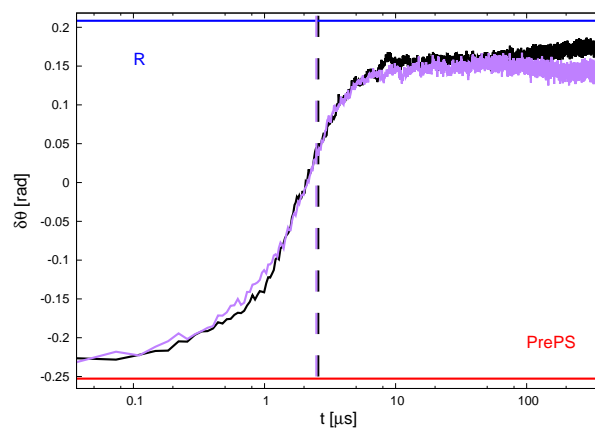
(a)



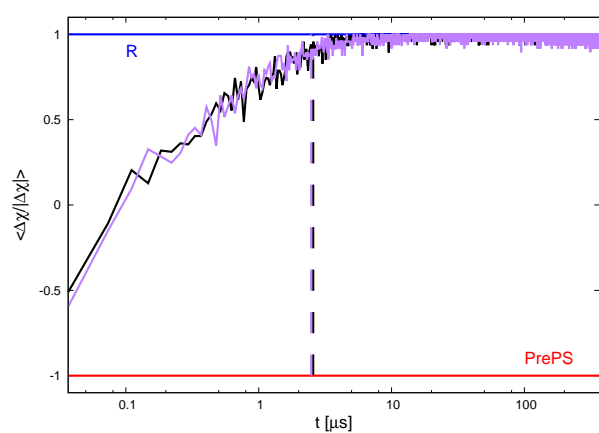
(b)



(c)



(d)



(e)

Figure S7: The movement of the converter during the PrePS $\rightarrow$ R transition. (Caption is in the following page).

Figure S7: (a) MVI in PrePS conformation. the red arrow shows the vector connecting N477 (black bead) to Y721 (red bead), and the green arrow shows the vector connecting N477 to C735 (green bead). The angle between F-actin (z axis) and the arrow connecting N477 to Y721 is smaller than the angle between F-actin and the N477-C735 arrow, that is  $\delta\theta < 0$ . (b) MVI in R conformation. Note that in this case  $\delta\theta > 0$ . (c) The movement of the geometric center of the converter. The black line indicates results obtained in the absence of a backward load, while the simulations carried out with a  $F=6\text{pN}$  force pulling on the lever arm are shown in purple. The continuous line shows the geometric center of the converter, averaged over all the uncoupled trajectories. The dashed line shows instead the average  $t_{\chi 1}$ . The red line reports the position of the geometric center found in the PrePS conformation, and the geometric center in the R state is shown in blue. (d) The angle showed in panels (a-b) as a function of time, averaged over all the uncoupled trajectories. The color code is the same as in panel (c). (e) The average over the trajectories of  $\Delta\chi/|\Delta\chi|$  as a function on time, where  $\Delta\chi = \chi(\text{R}) - \chi(\text{PrePS})$ , that is the difference between the structural overlap function to the R state and to the PrePS state.

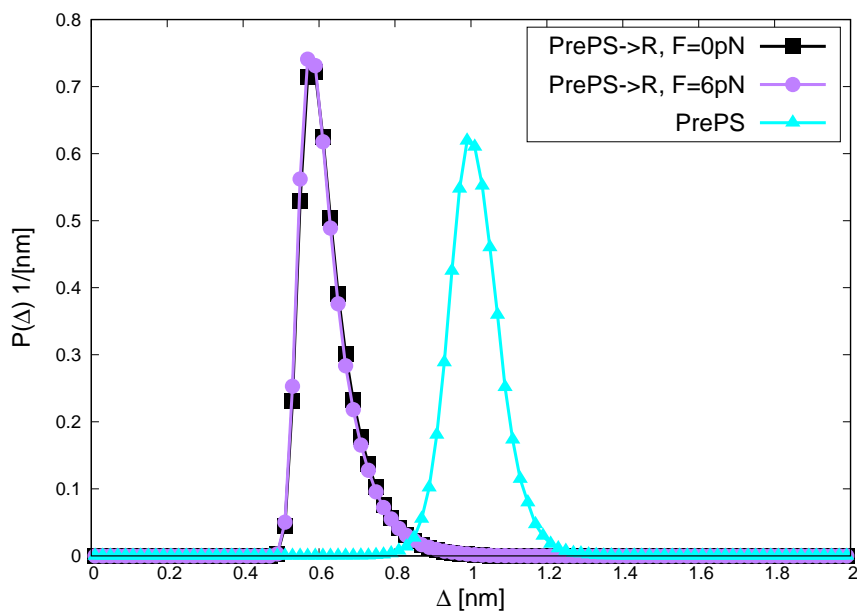
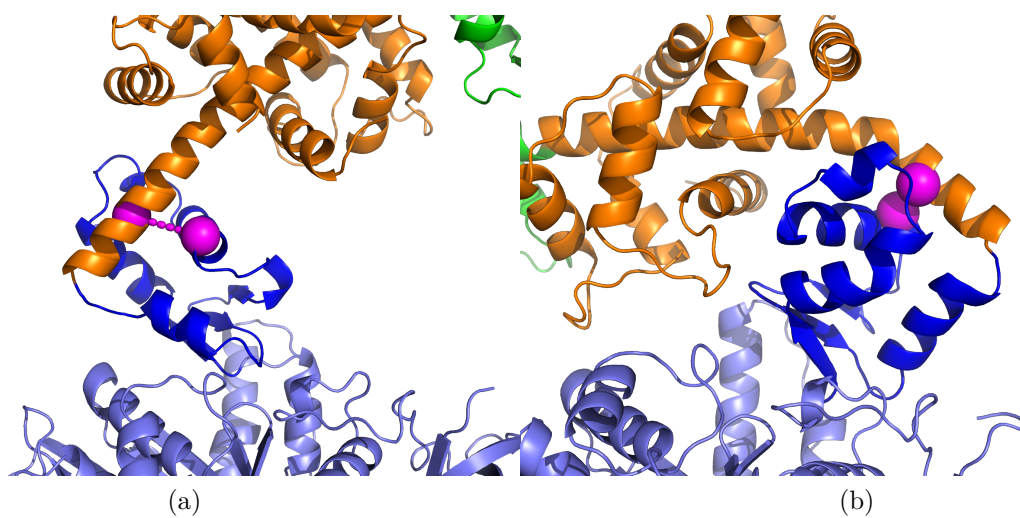


Figure S8: Formation of R-state contact between ins2 and the converter. (a) The magenta beads are A741 and V781 in the PrePS conformation. (b) Same as (a), but in the R state. (c) The figure shows the distribution of the distance  $\Delta$  between A741 and V781 for the simulations of the PrePS $\rightarrow$ R transition after  $\tau_{\chi_1}$  with and without backward load after as black squares and purple circles, respectively. As cyan triangles, we show the same distribution obtained from simulations of the PrePS state.

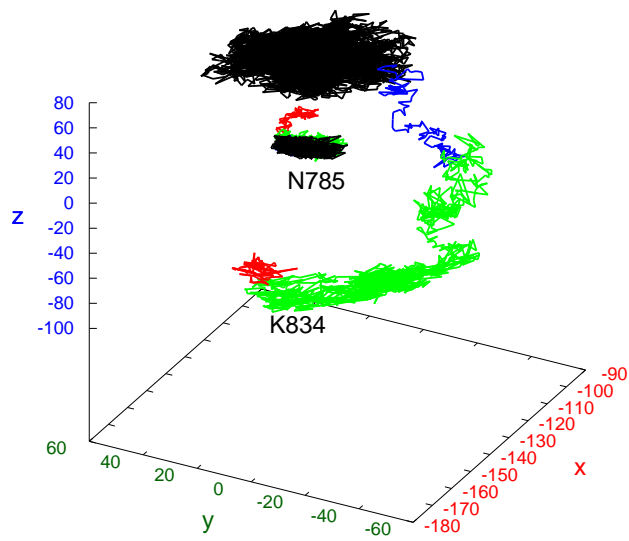


Figure S9: A representative trajectory monitoring the position of N785 and K834. The red portion of the trajectory is for  $t < \tau_{\chi_1}$ , the green for  $\tau_{\chi_1} \leq t < \tau_{\chi_2}$ , the blue for  $\tau_{\chi_2} \leq t < \tau_{\chi_3}$ , and the black for  $t \geq \tau_{\chi_3}$ . The scale on the right indicates the time spent in each portion of the trajectory.

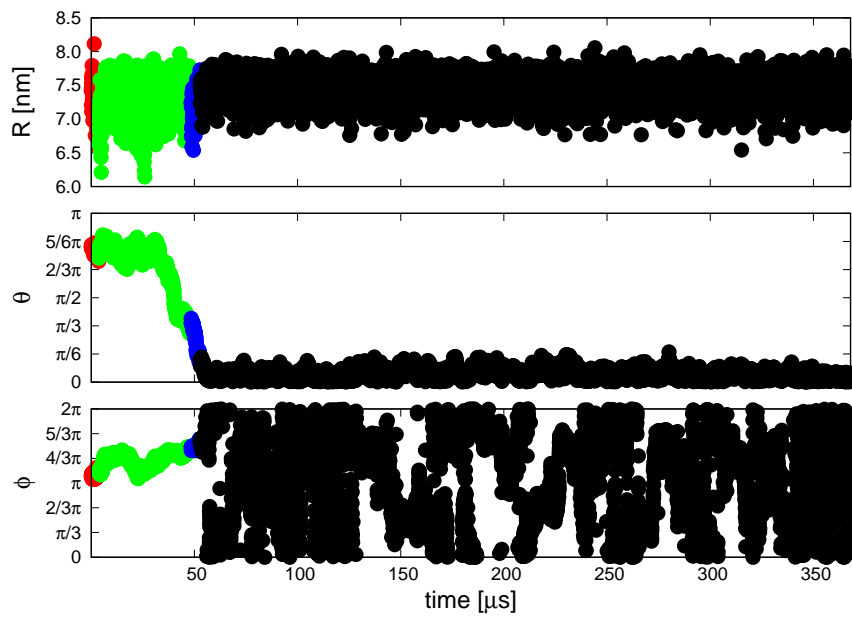


Figure S10: Uncoupled trajectory of the relative position of K834 with respect to N785 expressed in spherical coordinates. Top panel: the radius as a function of time. Middle panel: the angle  $\theta$  as a function of time. Bottom panel: the angle  $\phi$  as a function of time. The color code is the same as in Fig. S9.

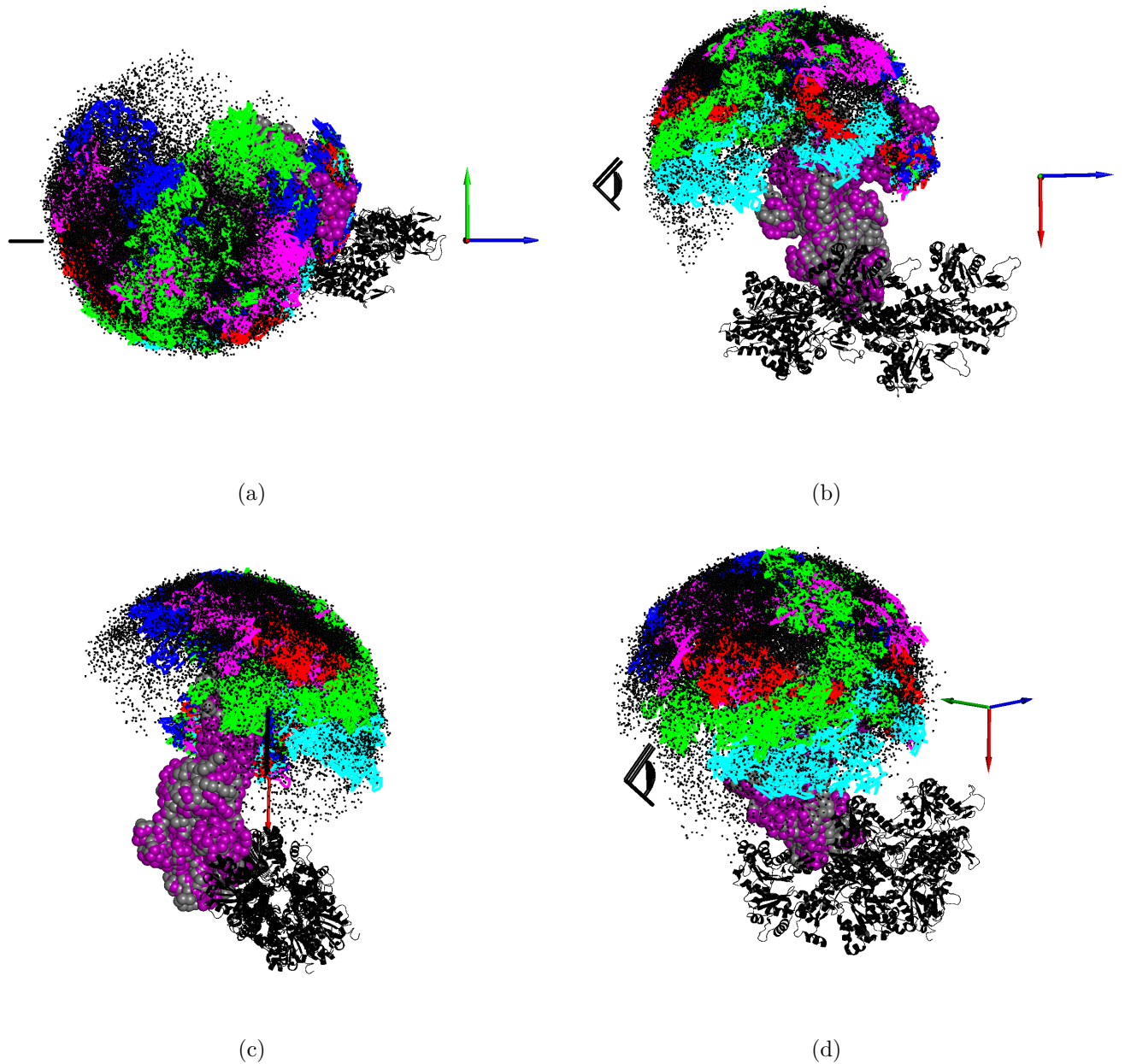


Figure S11: The movement of the lever arm during PrePS $\rightarrow$ R transition for uncoupled trajectories. In black cartoons we show F-actin from 1MVW [19]. MVI in PrePS and R conformation is shown as grey and purple spheres, respectively. The black dots represent the position of K834 in space during the 94 coupled trajectories. Five trajectories are shown as red, green, blue, magenta, and cyan lines. The point of view of the observer is identified by an eye. The cartesian axes are shown as arrows. (a) The perspective looking in the direction of the  $\hat{x}$ -axis. (b) Lever arm swing from the side of F-actin (looking towards the  $\hat{y}$ -axis). (c) The perspective of the observer, that is looking towards the  $\hat{z}$ -axis, along the actin filament. (d) A view from a side.

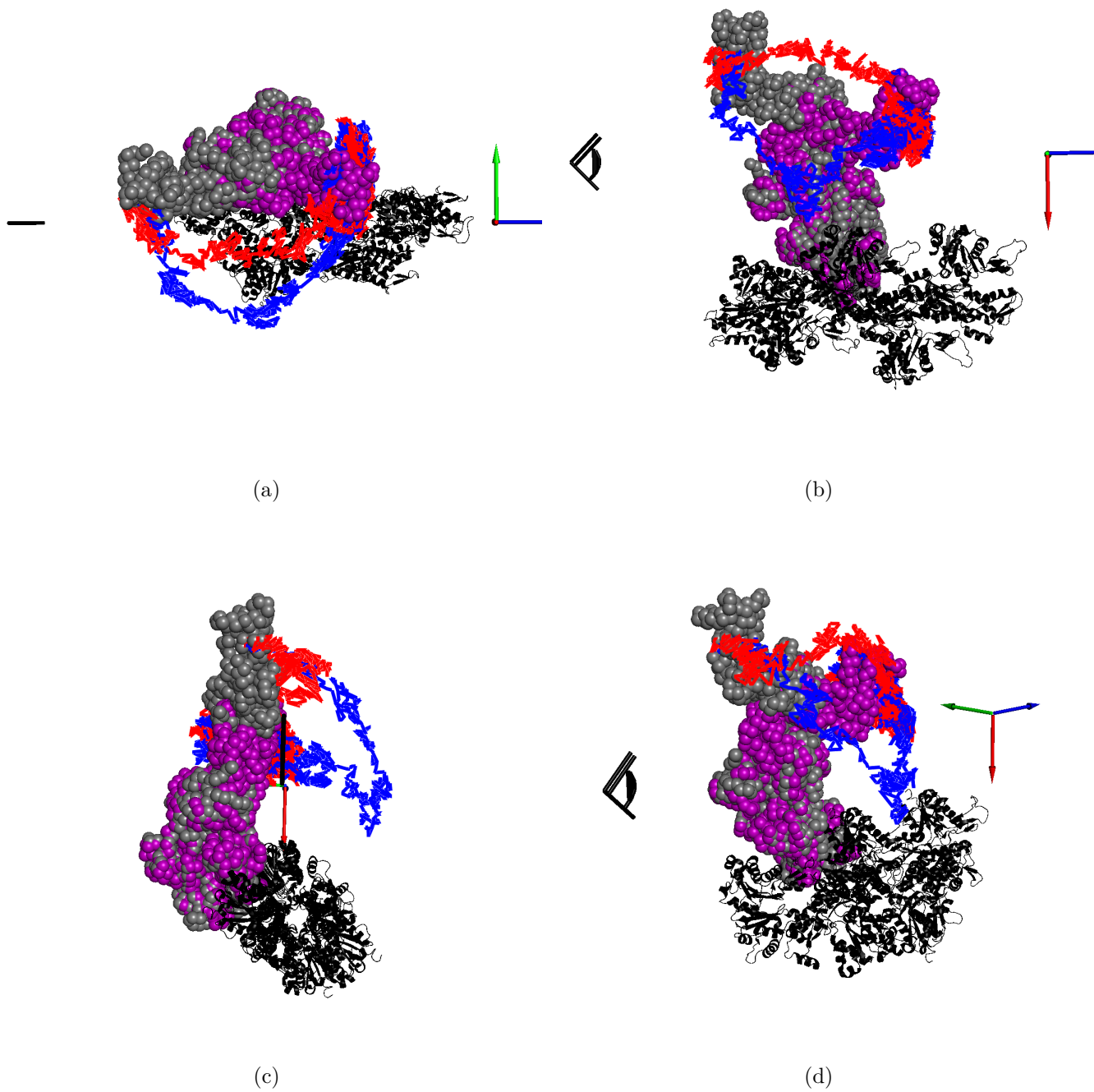


Figure S12: The movement of the lever arm during PrePS→R transition for coupled trajectories. Color code and panels are identical to those in Fig. S11.

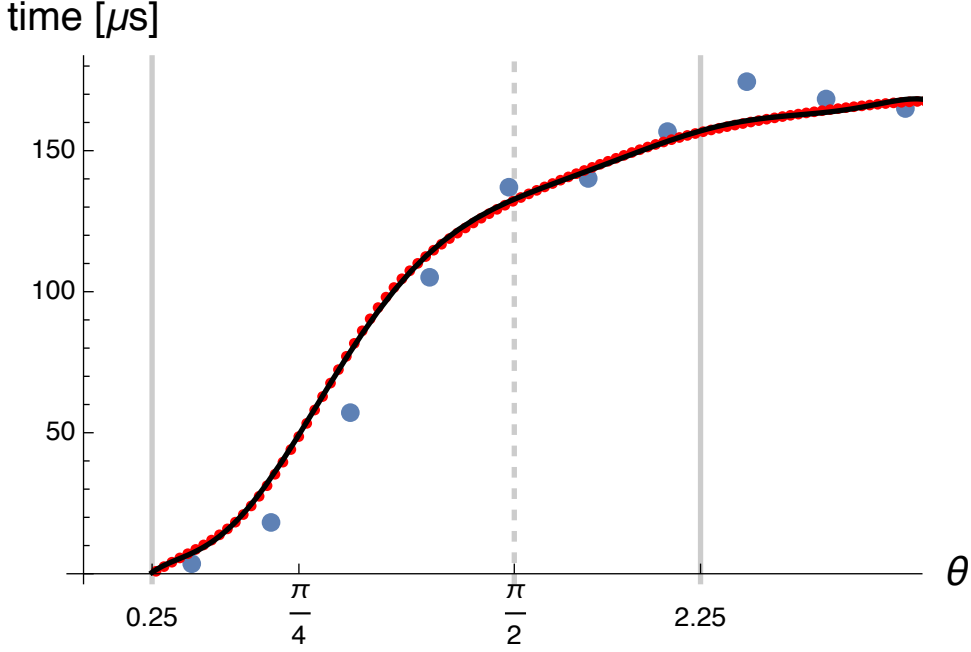


Figure S13: Comparison of MFPT from coarse grained simulations with the theoretical model. The blue points show the MFPT extracted from the coarse-grained simulations. The numerical solution of Eq. S15 at 100 values of  $\theta$  in the set  $[\theta_i, \pi]$  ( $\theta_i = 0.25\text{rad}$ ) is in red. The black line is a fit of the red points versus a eighth-order polynomial ( $a_0 + a_1x + a_2x^2 + a_3x^3 + a_4x^4 + a_5x^5 + a_6x^6 + a_7x^7 + a_8x^8$ , with  $a_0 = -0.85$ ,  $a_1 = 8.39$ ,  $a_2 = -32.10$ ,  $a_3 = 62.92$ ,  $a_4 = -64.07$ ,  $a_5 = 36.68$ ,  $a_6 = -11.96$ ,  $a_7 = 2.08$ ,  $a_8 = -0.15$ ). The black line is multiplied by the inverse of the diffusion coefficient  $1/D$ , which is fit versus the blue points to yield  $D \approx 0.011/\mu s$ . The continuous vertical lines show the injection point in the simulations and the absorbing boundary. Fit and numerical integration were performed with Mathematica [15].

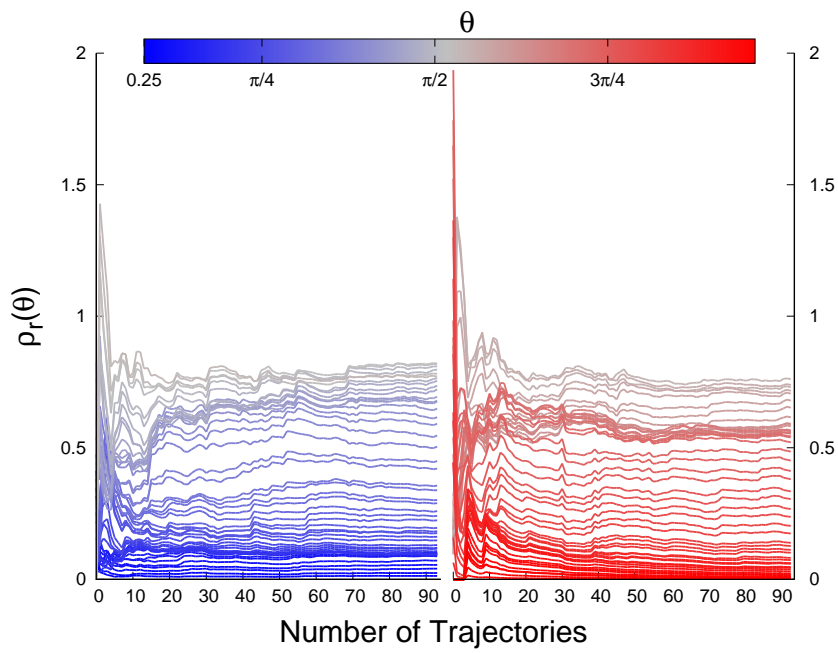


Figure S14: Convergence of  $\rho_r(\theta)$ . The probability distribution  $\rho_r(\theta)$  is shown as a function of the number of trajectories used to extract it. The different colors show the probability distribution computed at different  $\theta$ -values.

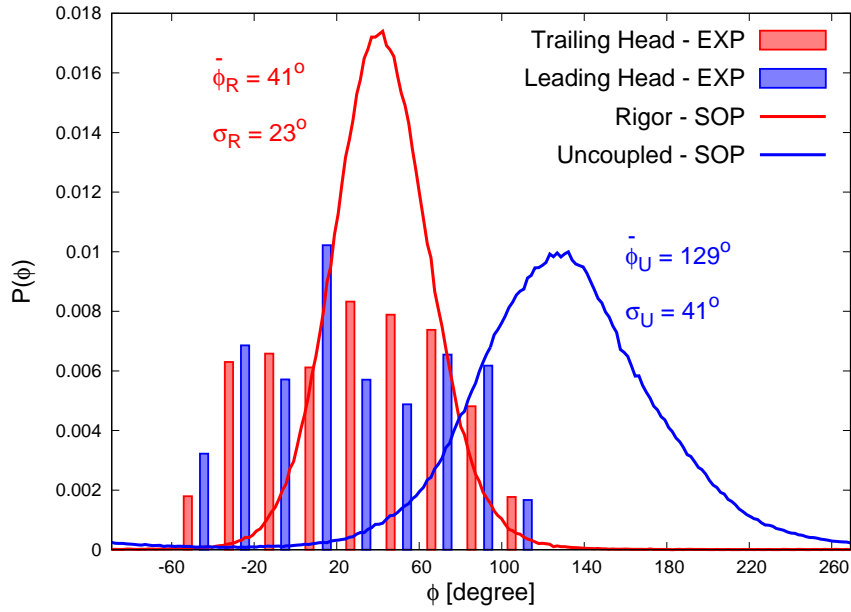


Figure S15: Comparison of azimuthal angle in simulations and experiments [11]. The histograms were extracted from Fig. 3 of [11]. Distribution of  $\phi$  ( $\alpha$  in [11]) of the trailing (red) and leading (blue) heads. The azimuthal angles from our simulations were shifted by  $-90^\circ$  to take care of the different definition of the axes in the paper and in [11]. The data from simulations were fit using normal distributions. The fit parameters are shown in the figure. The average of the distribution is denoted with a bar, the standard deviation is labeled as  $\sigma$ .

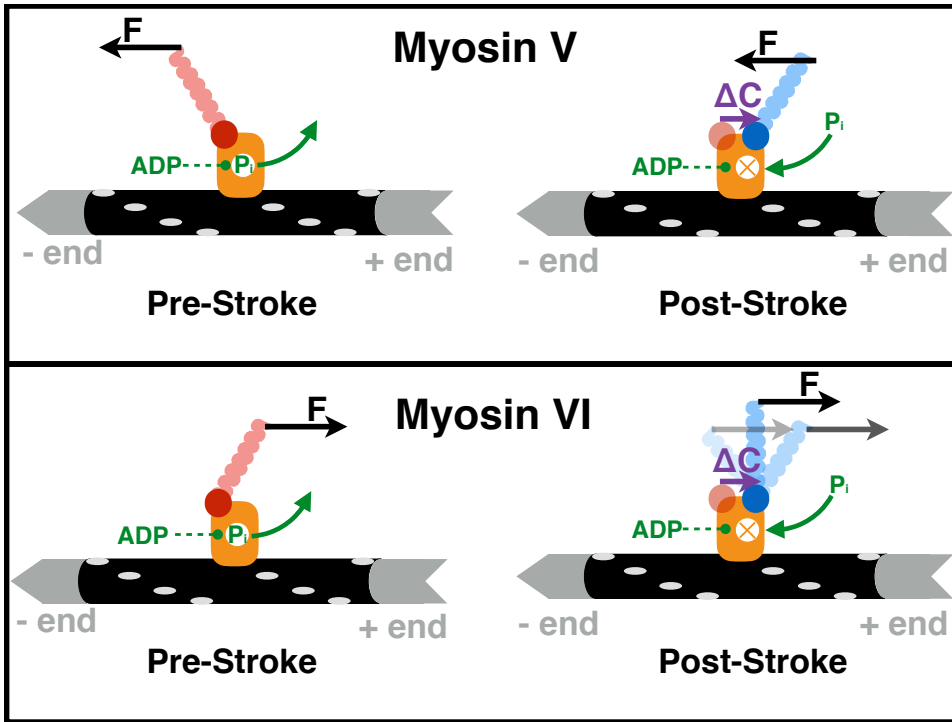


Figure S16: The effect of load on the rotation of the converter in plus-end and minus-end motors. In orange we show the motor domain, and in black F-actin. The purple arrow indicates the vector  $\Delta\vec{C}$  connecting the PrePS converter (red sphere) to the post-stroke converter (blue sphere). The black arrow shows the direction of the backward load  $\vec{F}$ . The top panel displays a cartoon of MV power stroke; MVI is shown in the bottom panel. In both the panels the pre-stroke conformation is on the left, the post-stroke conformation on the right. In the pre-stroke state  $P_i$  can escape from the binding site, and it cannot rebind in the post-stroke conformation. Note that  $\Delta\vec{C}$  and the resistive force,  $\vec{F}$ , are antiparallel in MV, and parallel in MVI. By comparing the pre- and post-stroke PDB structures of myosin II (another plus-end motor, like MV) [20] and MVI we get  $\Delta\vec{C} \cdot \vec{F}/(|\Delta\vec{C}||F|) \approx -0.99$  and  $\approx 0.99$ , respectively.

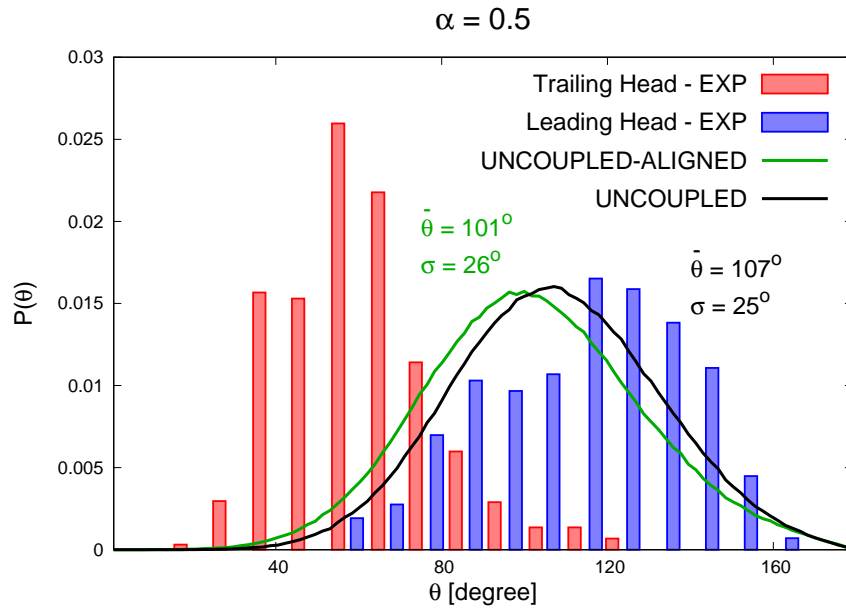


Figure S17: Comparison of simulations with experimental data from PolTIRF [11] after re-alignment of the motor domain. The data is the same as in Fig. 7a. We also present results obtained after re-alignment of the MVI motor domain to the myosin II from PDB 1MVW [19] (green curve). Both the green is in good agreement with the experiments (the width of the distribution is close to the one evaluated in [11]), suggesting that the details of the actomyosin interface might not affect our results significantly.

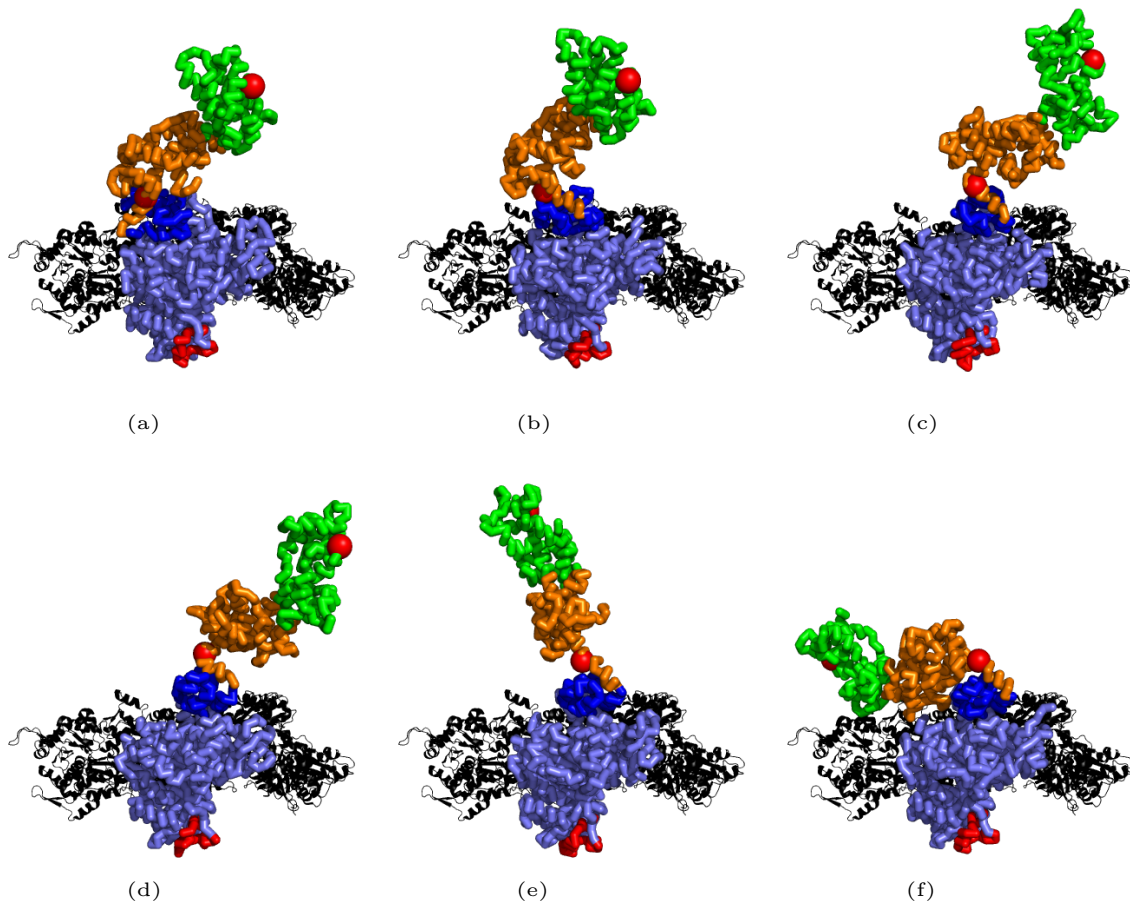


Figure S18: Images from an uncoupled trajectory in the absence of backward load. Different panels show the conformation at different times. (a)  $t \approx 0 \mu s$ , (b)  $t \approx 3 \mu s$ , (c)  $t \approx 11 \mu s$ , (d)  $t \approx 22 \mu s$ , (e)  $t \approx 44 \mu s$ , (f)  $t \approx 55 \mu s$ .

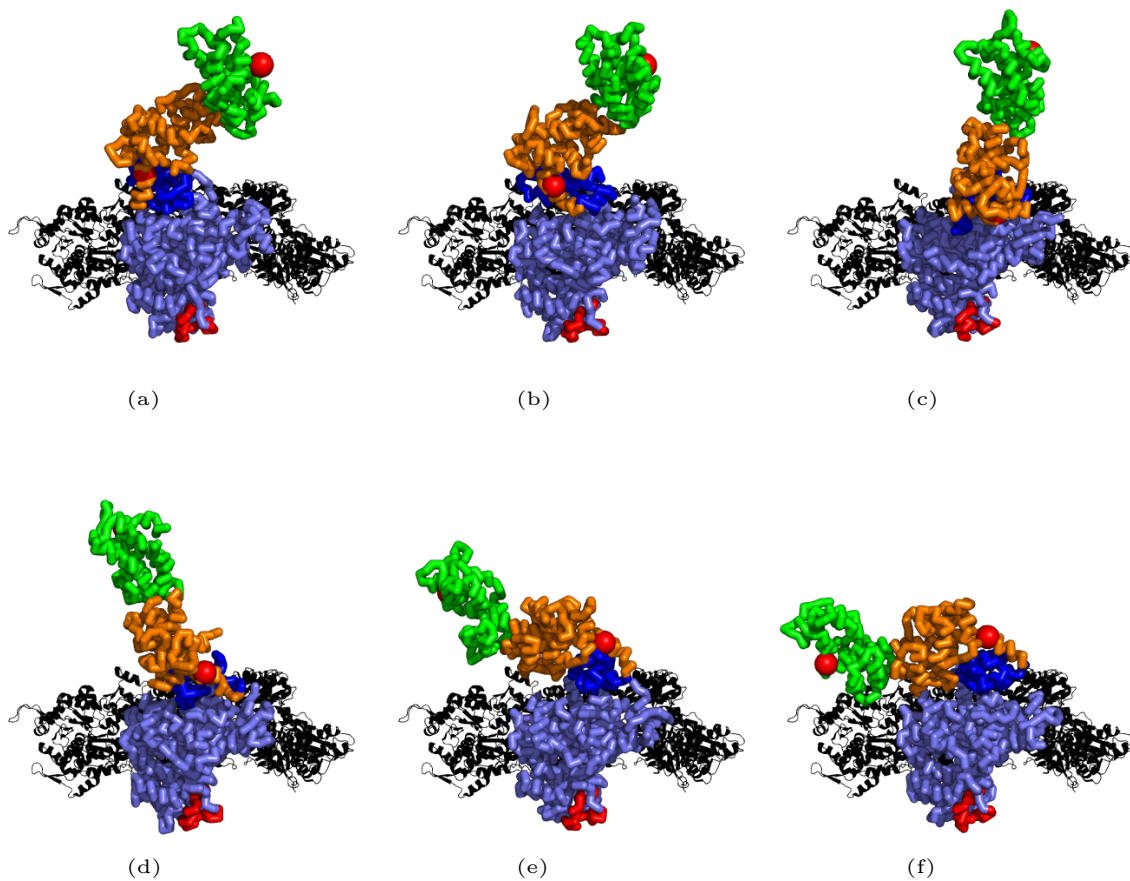


Figure S19: Images from a coupled trajectory in the absence of backward load. Different panels show the conformation at different times. (a)  $t \approx 0\mu s$ , (b)  $t \approx 3\mu s$ , (c)  $t \approx 6\mu s$ , (d)  $t \approx 11\mu s$ , (e)  $t \approx 15\mu s$ , (f)  $t \approx 22\mu s$ . Note the difference in time scale compared to Fig. S18: the image in panel (f) in this figure is taken at the same time as the image in panel (d).

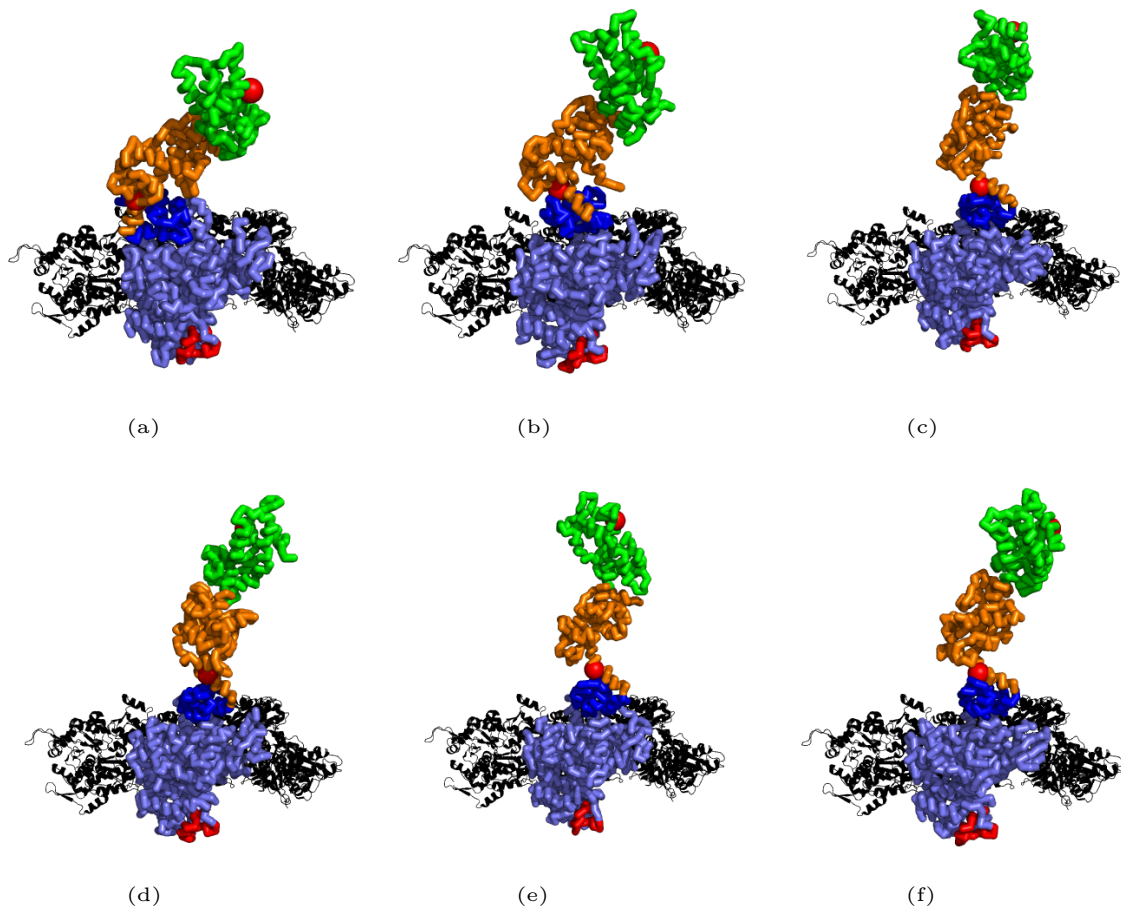


Figure S20: Images from an uncoupled trajectory in the presence of a 6pN backward load. Different panels show the conformation at different times. (a)  $t \approx 0\mu s$ , (b)  $t \approx 3\mu s$ , (c)  $t \approx 11\mu s$ , (d)  $t \approx 22\mu s$ , (e)  $t \approx 44\mu s$ , (f)  $t \approx 55\mu s$ . The time frames are the same as in Fig. S18.

$\epsilon_{\text{NAT}}$	2 kcal/mol
$\epsilon_{\text{NNAT}}$	1 kcal/mol
$\sigma$	3.8Å
$k_F$	20 kcal/(mol Å <sup>2</sup> )
$R_F$	2Å
$R_C$	8Å

Table S1: Parameters for SOP simulations.

ID of Gaussian	$a_i$	$\mu_i$	$\sigma_i$
1	-3.500	0.000*	0.813
2	0.690	0.640	0.150
3	1.400	0.968	0.288
4	-0.501	1.240	0.161
5	-0.290	1.600	0.141
6	-0.080	1.850	0.100
7	-0.110	2.240	0.100
8	2.300	$\pi^*$	0.410

Table S2: Parameters for the fitting of the free energy  $F(\theta)$ , see equation S12. The parameters labeled with the symbol “\*” were not fitted. All parameters are dimensionless. The parameters  $a_i$  should be multiplied by  $k_B T$  to get the corresponding energy.

## References

- [1] Changbong Hyeon, George H Lorimer, and D Thirumalai. Dynamics of allosteric transitions in GroEL. *Proceedings of the National Academy of Sciences*, 103(50):18939–18944, 2006.
- [2] Riina Tehver and D Thirumalai. Rigor to post-rigor transition in myosin V: link between the dynamics and the supporting architecture. *Structure*, 18(4):471–481, 2010.
- [3] Zhechun Zhang and D Thirumalai. Dissecting the kinematics of the kinesin step. *Structure*, 20(4):628–640, 2012.
- [4] David E Shaw, Ron O Dror, John K Salmon, JP Grossman, Kenneth M Mackenzie, Joseph A Bank, Cliff Young, Martin M Deneroff, Brannon Batson, Kevin J Bowers, Edmond Chow, Michael P Eastwood, Douglas J Ierardi, John L. Klepeis, Jeffrey S. Kuskin, Richard H. Larson, Kresten Lindorff-Larsen, Paul Maragakis, Mark A. Moraes, Stefano Piana, Yibing Shan, and Brian Towles. Millisecond-scale molecular dynamics simulations on anton. In *High Performance Computing Networking, Storage and Analysis, Proceedings of the Conference on*, pages 1–11. IEEE, 2009.
- [5] Paola Llinas, Tatiana Isabet, Lin Song, Virginie Ropars, Bin Zong, Hannah Benisty, Serena Sirigu, Carl Morris, Carlos Kikuti, Dan Safer, H. Lee Sweeney, and Anne Houdusse. How actin initiates the motor activity of myosin. *Developmental cell*, 33(4):401–412, 2015.
- [6] Donald L Ermak and JA McCammon. Brownian dynamics with hydrodynamic interactions. *The Journal of chemical physics*, 69(4):1352–1360, 1978.
- [7] Daan Frenkel and Berend Smit. *Understanding molecular simulation: from algorithms to applications*, volume 1. Academic press, 2001.

- [8] Thomas Veitshans, Dmitri Klimov, and Devarajan Thirumalai. Protein folding kinetics: timescales, pathways and energy landscapes in terms of sequence-dependent properties. *Folding and Design*, 2(1):1–22, 1997.
- [9] Jorge Nocedal and Stephen Wright. *Numerical optimization*. Springer Science & Business Media, Spring Street, NY, USA, 2006.
- [10] Yusuke Oguchi, Sergey V Mikhailenko, Takashi Ohki, Adrian O Olivares, Enrique M De La Cruz, and Shin’ichi Ishiwata. Load-dependent adp binding to myosins v and vi: implications for subunit coordination and function. *Proceedings of the National Academy of Sciences*, 105(22):7714–7719, 2008.
- [11] Yujie Sun, Harry W Schroeder, John F Beausang, Kazuaki Homma, Mitsuo Ikebe, and Yale E Goldman. Myosin VI walks “wiggly” on actin with large and variable tilting. *Molecular cell*, 28(6):954–964, 2007.
- [12] Julie Ménétreay, Paola Llinas, Monalisa Mukherjea, H Lee Sweeney, and Anne Houdusse. The structural basis for the large powerstroke of myosin VI. *Cell*, 131(2):300–308, 2007.
- [13] Julie Ménétreay, Tatiana Isabet, Virginie Ropars, Monalisa Mukherjea, Olena Pylypenko, Xiaoyan Liu, Javier Perez, Patrice Vachette, H Lee Sweeney, and Anne M Houdusse. Processive steps in the reverse direction require uncoupling of the lead head lever arm of myosin VI. *Molecular cell*, 48(1):75–86, 2012.
- [14] Qi Zhang, Jasna Brujić, and Eric Vanden-Eijnden. Reconstructing free energy profiles from nonequilibrium relaxation trajectories. *Journal of Statistical Physics*, 144(2):344–366, 2011.
- [15] Inc. Wolfram Research. *Mathematica*. Champaign, Illinois, version 10.3 edition, 2015.
- [16] Robert Zwanzig. *Nonequilibrium statistical mechanics*. Oxford University Press, USA, Oxford, UK, 2001.

- [17] James R Sellers and Claudia Veigel. Direct observation of the myosin-Va power stroke and its reversal. *Nature structural & molecular biology*, 17(5):590–595, 2010.
- [18] Sarah F Wulf, Virginie Ropars, Setsuko Fujita-Becker, Marco Oster, Goetz Hofhaus, Leonardo G Trabuco, Olena Pylypenko, H Lee Sweeney, Anne M Houdusse, and Rasmus R Schröder. Force-producing adp state of myosin bound to actin. *Proceedings of the National Academy of Sciences*, page 201516598, 2016.
- [19] Li Fan Chen, Hanspeter Winkler, Michael K Reedy, Mary C Reedy, and Kenneth A Taylor. Molecular modeling of averaged rigor crossbridges from tomograms of insect flight muscle. *Journal of structural biology*, 138(1):92–104, 2002.
- [20] A Houdusse, Andrew G Szent-Györgyi, and Carolyn Cohen. Three conformational states of scallop myosin s1. *Proceedings of the National Academy of Sciences*, 97(21):11238–11243, 2000.